The Thesis Committee for Alexander Gary Fay
Certifies that this is the approved version of the following thesis:

Mitigation of the Radioxenon Memory Effect in Beta-Gamma Detector Systems by Deposition of Thin Film Diffusion Barriers on Plastic Scintillator

APPROVED BY
SUPERVISING COMMITTEE:

Supervisor: _____

Steven R.F. Biegalski

_____

Derek Haas

Mitigation of the Radioxenon Memory Effect in Beta-Gamma Detector Systems by Deposition of Thin Film Diffusion Barriers on Plastic Scintillator

by

Alexander Gary Fay, B.S.

Thesis

Presented to the Faculty of the Graduate School of

The University of Texas at Austin

in Partial Fulfillment

of the Requirements

for the Degree of

Master of Science in Engineering

The University of Texas at Austin

December 2010

Dedication

For my family,

which has given me every opportunity to pursue every opportunity.

Acknowledgements

I would like to acknowledge Dr. Steven Biegalski for his invaluable guidance and support throughout this project. I would also like to thank the staff of the Nuclear Engineering Teaching Laboratory at the University of Texas at Austin for making this research possible. Finally, I would like to thank my collaborators at Uppsala University and FOI in Sweden for their assistance with this project.

This work was done with financial support from Department of Defense, Space and Missile Defense Command, Nuclear Arms Control Technology Program under a contractual arrangement with Pacific Northwest National Laboratory, Richland, Washington.

December 3, 2010

Mitigation of the Radioxenon Memory Effect in Beta-Gamma Detector Systems by Deposition of Thin Film Diffusion Barriers on Plastic Scintillator

Alexander Gary Fay, MSE

The University of Texas at Austin, 2010

Supervisor: Steven R.F. Biegalski

The significance of the radioxenon memory effect in the context of the International Monitoring System of the Comprehensive Nuclear-Test-Ban Treaty is introduced as motivation for the project. Existing work regarding xenon memory effect reduction and thin film diffusion barriers is surveyed. Experimental techniques for radioxenon production and exposure, as well as for thin film deposition on plastic by plasma enhanced chemical vapor deposition (PECVD), are detailed. A deposition rate of 76.5 nm min^{-1} of SiO_2 is measured for specific PECVD parameters. Relative activity calculations show agreement within 5% between identically exposed samples counted on parallel detectors. Memory effect reductions of up to 59±1.8% for 900 nm SiO_2 films produced by plasma enhanced chemical vapor deposition and of up to 77±3.7% for 50 nm Al_2O_3 films produced by atomic layer deposition are shown. Future work is suggested for production of more effective diffusion barriers and expansion to testing in operational monitoring stations.

Table of Contents

List of Tables

List of Figures

Chapter 1: Introduction

1.1 Background

The efforts in support of nuclear nonproliferation began with the advent of nuclear weapons development in the United States. Although initial development of applications of nuclear power occurred primarily in the United States and Russia, both countries promptly exported peaceful nuclear technology to allies around the world. With the rapid growth of nuclear technology and the propagation of nuclear materials throughout the world, the concern that such technology and materials could be misused also spread. Born out of this concern was the Nonproliferation Treaty (NPT) of 1968. The NPT distinguished weapons states, the five countries that had nuclear weapons programs, from non-weapons states, countries party to the NPT that had not developed nuclear weapons. The purpose of the NPT was to discourage the further development and spread of nuclear weapons programs by non-weapons states in return for assistance, from the weapons states, in developing peaceful nuclear technology. However, concerns about the development of a nuclear weapon via diversion of fissile materials by states or theft of fissile materials by non-states persisted. Although the NPT encourages progress towards disarmament, it does not specifically address the use of nuclear weapons [1].

The 1974 weapons test by India, a non-NPT country, reignited fears about continued development of nuclear weapons. Concurrent weapons testing moratoriums in the United States, Russia, and the United Kingdom, along with a series of committee and working group meetings, provided the necessary

groundwork to begin official negotiations on a weapons test treaty. In 1996, the Comprehensive Nuclear-Test-Ban Treaty (CTBT) was opened for signature.

The CTBT prohibits the use of nuclear weapons in all applications, civilian and militaristic. The treaty does not distinguish between underground, underwater, or atmospheric detonations, thus nuclear weapons tests are comprehensively prohibited as well. The treaty further prohibits any "encouragement of or participation in" a nuclear explosion and outlines the procedure for addressing violations [2]. As of October 2010, 165 states have signed the treaty and 97 have ratified it. Of the five NPT weapons states, France, Russia, and the United Kingdom have signed and ratified the treaty, while the United States and China are signatories but have not ratified [3].

In order for the treaty to enter into force, a satisfactory verification regime must be established. This regime for the CTBT consists of the International Monitoring System (IMS), the International Data Center (IDC), and a variety of direct inspection measures. The IMS stands as a network of monitoring stations that report data to the IDC. The IDC collects the IMS data and makes it available to any CTBT state. Member states are then responsible for data analysis.

The IMS is composed of four monitoring technologies: seismic, hydroacoustic, infrasound, and radionuclide. Seismic stations monitor the seismic waves produced in an underground nuclear explosion. This seismic information can be used to determine the strength of an event and the distributed network of monitoring stations is capable of identifying the location of an event. The fast seismic response from an underground or atmospheric explosion allows this type

of monitoring to provide information to the IDC within seconds of an explosion [4]. Hydroacoustic monitoring stations are able to detect the acoustic response of a nuclear explosion as the acoustic wave travels through the ocean. Similar to seismic monitoring techniques, hydroacoustic monitoring is capable of locating the source of the signal as well as distinguishing between explosions and earthquakes [4]. Infrasound stations monitor for changes in atmospheric pressure in order to identify atmospheric nuclear explosions. These pressure changes are produced occasionally in underground explosions as well and are detected as acoustic signals at lower frequency than detectable by the hydroacoustic network. The infrasound network further supplements the capabilities of the seismic and hydroacoustic networks to locate the source of the explosion.

The only IMS monitoring technique not based on waveform analysis is radionuclide monitoring. Radionuclide stations detect radioactive fission products created in a nuclear explosion. Many of these fission products will escape into the atmosphere as a result of the venting of the explosion. The response time of radionuclide signals from an explosion is longer than that of seismic or acoustic signals and the source location is more difficult to determine considering the atmospheric transport of the fission products [4]. However, proper containment of an explosion is difficult, even underground, thus radionuclide monitoring can achieve low detection thresholds.

The radionuclide network consists of 80 radionuclide monitoring stations. Of these 80 stations, 40 have been developed with additional monitoring capabilities as part of the International Noble Gas Experiment [5]. The location of these stations is indicated in Figure 1.1.

Figure 1.1. Distribution of deployed and planned IMS radionuclide stations with radioxenon monitoring capabilities [5].

The International Noble Gas Experiment (INGE) was created as a means of secondary detection of radionuclide signals from nuclear weapons detonations. The INGE stations continuously collect radioactive xenon from the atmosphere and monitor isotopic ratios of ^{131m}Xe, ^{133}Xe, ^{133m}Xe, and ^{135}Xe. The ratios of these isotopes can be used to distinguish radioxenon produced in a weapons detonation from radioxenon produced from the other major sources: medical isotope production facilities, nuclear reprocessing plants and nuclear power reactors [7].

Station designs from four countries have been developed for use in the INGE network. The Automated Radioxenon Sampler-Analyzer (ARSA) was developed by Pacific Northwest National Laboratory in the United States. The Systeme de Prelevement d'Air Automatique en Ligne avec l'Analyse Radioxenon

Atmospheriques (SPALAX) was developed by the Departement Analyse, Surveillance, Environnement du CEA in France. The Automatic Radioanalyzer for Isotopic Xenon (ARIX) was developed by the Khlopin Radium Institute in Russia. The Swedish Automated Unit for Noble Gas Acquisition (SAUNA) was developed by the Totalförsvarets Forskningsinstitut (FOI) in Sweden [6].

1.2 Literature Review

1.2.1 Xenon Monitoring

Shortly after the signing of the CTBT in 1996, work began to establish the verification regime for the treaty. Radioactive isotopes of xenon were identified as fission products of interest for monitoring purposes and the requirements for a viable network of radioxenon monitoring stations were outlined [7]. Specifically, stations would have to be autonomous with only intermittent maintenance requirements, capable of twice-a-day measurements of the isotopes of interest, able to achieve sensitivity many times higher than current technology, and capable of transmitting data back to the then-proposed IDC. Subsequently, four organizations began development of radioxenon monitoring station designs, as outlined in the introduction to this chapter.

Testing of the four radioxenon monitoring station designs has been conducted both on an individual basis and as a comparison between systems. Development and testing of the Automated Radioxenon Sampler/Analyzer (ARSA) was initially reported in 1998 [8]. The ARSA station extracts xenon from intake air via a series of molecular sieves and charcoal traps. The xenon is fed into a plastic scintillator cell for beta-gamma coincidence counting, measured

in a residual gas analyzer, then stored in an archiving bottle. Prototypes of the ARSA detector achieved sensitivities of 0.1 mBq m^{-3} [9]. Sensitivities are given in units of detectable activity per unit volume air collected.

Initial testing of the Systeme de Prelevement Automatique en Ligne avec L'Analyse du Xenon (SPALAX) was reported in 2004 [10]. The SPALAX station purifies xenon from the atmosphere by use of activated charcoal and diffusion membranes. Quantification of the radioxenon is conducted on a high-purity germanium (HPGe) detector, thus the minimum detectable activity (MDA) is calculated solely from X-ray and gamma ray signals. Initial incarnations of the SPALAX achieved an MDA of 0.7 mBq m^{-3} for ^{131m}Xe and 0.9 mBq m^{-3} for ^{133m}Xe [10].

The Russian ARIX detector was presented with initial measurements in 2005 [11]. Molecular sieves and activated charcoal traps were utilized for xenon purification and radioxenon measurement was accomplished using beta-gamma coincidence counting with a plastic scintillator cell. The initial MDA for the ARIX was reported at 0.5 mBq m^{-3}.

Testing of the Swedish Automated Unit for Noble Gas Acquisition (SAUNA) was initially reported in 2003 [12]. Xenon purification was achieved at room temperature using activated charcoal then initial quantification of the purified xenon was done using a gas chromatograph. Beta-gamma coincidence measurements of radioxenon activity were conducted in a plastic scintillator cell similar to those used in the ARSA and ARIX. MDA from 0.57 mBq m^{-3} to 0.93 mBq m^{-3} were achieved in the initials tests, leaving all four detector designs in

compliance with the IMS mandated MDA as reported by the designing organizations.

It is important to note that station designs varied amongst each other with respect to counting techniques, purification processes, and cycle times. In order to ensure the capability of each design to meet the requirements of the IMS and identify potential issues, an intercomparison of the four systems was conducted and reported in 2004 [6]. The single-site, 400 day comparison of the four systems was conducted in 2000 - 2001. Independent radioxenon measurements were conducted at the site in Freiburg, Germany. In addition to ongoing atmospheric monitoring and analysis of archived samples by all detectors, known activities of xenon isotopes were introduced to the system in a series of "spike tests."

Large variations in atmospheric radioxenon activity (two orders of magnitude) were seen over the course of the test. These variations were attributed to local emission sources, primarily nuclear power facilities. Discrepancies in activity measurements between detectors in the atmospheric monitoring tests and spike tests were also seen, however the magnitude of these discrepancies was shown to be significantly lower than the expected signal from a nuclear detonation.

Collectively, the MDA of a network composed of the four tested designs was shown to be viable over a range of activities from 1 mBq m^{-3} to 100 mBq m^{-3}, which was the maximum activity seen in the intercomparison. The MDA for the network was shown to be 0.1 - 1 mBq m^{-3} and in compliance with the IMS requirements as reported by an independent organization [6].

Deployment and field testing was conducted following the results of the INGE station intercomparison. Commercial versions of the ARIX, SPALAX, and SAUNA were manufactured and deployed as a network of 16 INGE stations. Uptime of the network was 74.1% of cumulative system hours over the course of the 48-month test [13]. Primary causes of downtime were HPGe cooling system maintenance, software malfunction, and gas processing equipment malfunction. The atmospheric radioxenon MDA had been reduced to 0.2 - 0.6 mBq m^{-3} on the SPALAX system, 0.2 - 0.4 mBq m^{-3} on the ARIX system, and 0.2 - 0.3 mBq m^{-3} on the SAUNA system.

The 16 radioxenon monitoring stations tested at this time [13] serve as the foundation for the planned network of 40 stations.

1.2.2 Xenon Memory Effect in Application

The radioxenon memory effect incurs difficulties in a variety of applications. It is identified as an issue in discussion of detector design and performance [14,15]. Models of beta-gamma coincidence systems have been designed to account for the memory effect [16,17]. Development of new detector designs focuses on minimizing the impact of the memory effect [18,19]. Additionally, the memory effect has been discussed in the context of the INGE detector designs [13,20,21], with initial measurements suggesting 5% memory for an 8-hour background following evacuation after a 24-hour count [22]. Stable xenon memory effect issues have been identified in mass spectrometry applications as well [23,24].

1.2.3 Previous Memory Effect Work

Previous efforts to mitigate the radioxenon memory effect in counting applications are limited. Metallization of the plastic scintillator and use of inorganic scintillator materials have been explored [25]. Chrome and copper were identified as unviable materials for metallization due to low reflectivity and poor mechanical properties when coated onto the scintillator surface. Aluminum was shown to reduce the memory effect by 80-86%. The inorganic scintillator was shown to have very low susceptibility to xenon permeation. Further work suggested by this reference includes optimization of the inorganic scintillator cell geometry and further quantification of aluminized cell performance.

1.2.4 PECVD on Plastic

Initial research on the use of plasma enhanced chemical vapor deposition (PECVD) for SiO_2 deposition was reported in 1981 [26,27] and low-temperature deposition (as low as 275C) research began shortly thereafter [28]. Room temperature PECVD techniques, with a focus on achieving high quality films by varying PECVD parameters to account for the very low temperatures, were reported in 1996 [29]. The deposition rate of SiO_2 was shown to increase as substrate temperature decreased, however a higher abundance of reaction precursors and products in the film was observed for silicon reactant gas flow rates comparable to high temperature PECVD processes. Reduction of this flow rate with respect to the carrier gas flow rate allowed for film qualities approaching those manufactured as higher temperatures.

The chemical processes relevant to the production of SiO_2 in PECVD reactors have been reviewed [30]. A more specialized investigation of the mechanical properties of SiO_2 films deposited on polymers was conducted in 1999 [31]. Diffusion barrier performance as a function of various PECVD parameters (pressure, power, gas flow rates) has been previously explored [32,33]. Research on the effects of PECVD power variations on substrate temperature, an important consideration in temperature sensitive applications, was conducted in these references as well. Research regarding SiO_2 manufacturing at low temperatures with a variety of gas mixtures is widely available in the literature. An overview of plasma dynamics in deposition applications, reactor architecture, thin film properties, and plasma effects on polymers is given in the reference by D'Agostino [34].

1.2.5 Inert Gas Transport

Observation of gas transport through polymers was recorded as early as 1829 when Graham observed the inflation of a rubber balloon in the presence of CO_2 [35]. Development of a wide array of polymers for commercial and industrial applications, including polyvinyltoluene (PVT), has led to research into the gas permeability of such materials.

Initial identification and quantification of the permeability of polyvinyltoluene with regards to inert gases was conducted as early as 1960. Permeability values for N_2, He, O_2, expressed in units of mL cm^{-2} cm^{-1} s^{-1} $cmHg^{-1}$ were calculated as an initial means of quantification [36].

The diffusion of noble gas molecules in a polymer matrix has been previously simulated in a molecular dynamics (MD) model as a series of hops by gas molecules between polymer sites, or traps [37]. Temperature dependency of the polymer in the model has been further explored by Takeuchi in 1991 [38,39], however most relevant to plastic scintillator application in beta-gamma systems is the modeling of diffusion in glassy polymers, or polymers below glass transition temperature [40]. The hop and trap model has since been shown to be in agreement with experimental results [41-43].

A general treatment of the physics of diffusion through polymers, including diffusion coefficient calculation techniques for comparison with experimental values, was given in 1994 [44]. A more exhaustive review of the various mathematical diffusion models, including development of diffusion theory derived from Fick's Law, was conducted in 2001 [45]. Of note in this reference is the observation:

> The transport mechanisms in polymers at a molecular level are not completely understood when $T < T_g$ [where T_g is the glass transition temperature of the polymer]. All the models proposed in the literature are phenomenological and contain one or several adjustable parameters which should be determined experimentally and are suitable only to a limited number of systems.

A corresponding experimental treatment of the discussion in this reference was provided [46]. Published experimental work on xenon diffusion in engineering applications is limited. Xenon diffusion through porous media has been explored using magnetic resonance imaging techniques [47]. Radioxenon diffusion through polycarbonates has also been tested [48]. This reference includes solutions for the

time-dependent activity of radioactive noble gas concentrations diffusing through a variety of polymer geometries.

Further discussion of general models for gas transport in polymers, transport models in specific industry-relevant polymers, and physical dependencies of the diffusion coefficient is widely available in the literature.

1.2.6 Gas Diffusion Barriers

Gas diffusion barrier technology, specifically technology based on materials and techniques explored in this thesis, is abundant in a variety of industries. Thus the literature regarding barrier properties and performance is extensive. Relevant applications include plasma deposited SiO barriers on polyester bottles [49] and the use of Al_2O_3-SiO_2 bilayer barriers [50] for plastic wrapping material. The properties of Al_2O_3-SiO_2 bilayers have been further explored [51].

Monolayers of both SiO_2 and Al_2O_3 have been utilized as gas diffusion barriers as well. Substantial reductions (10x - 150x) in O_2 diffusion were shown for SiO_2 films [32], along with reporting of morphological studies of high performing barriers. Exploration of the critical thickness of SiO_2 barriers, as well as the thickness dependence of the refractive index, has been conducted [33].

Initial investigations of the barrier properties of low temperature ALD produced Al_2O_3 barriers were conducted in 2004 [52]. Since then, Al_2O_3 barriers have been characterized for applications such as liquid crystal display coating and food packaging [53]. Deposition on polymers has also been specifically investigated [54].

Appreciable work has been done regarding xenon, and even radioxenon, barrier properties of biological materials relevant to the medical industry. Unfortunately the literature focused on the interaction of aforementioned diffusion barriers with xenon or other noble gases in engineering applications appears to be limited.

1.3 Problem Statement

The establishment of a rigorous verification regime is necessary for the Comprehensive Nuclear-Test-Ban Treaty to enter into force. A crucial element of this regime, the International Monitoring System, utilizes radioxenon monitoring technology as a means of verifying nuclear weapons detonation. In order to produce trustworthy data on atmospheric radioxenon concentration, the IMS requires monitoring stations be capable of autonomous operation and low minimum detectable activity.

The radioxenon memory effect inhibits compliance with both of these IMS requirements. Although background spectra collection integrated with the radioxenon measurement process currently accounts for the effect to an extent, the minimum detectable activity is still reduced. Thus, a solution to passively mitigate the radioxenon memory effect is optimal.

1.4 Project Goals

There were three primary goals for this project:

1. Develop an experimental procedure for radioxenon exposure and construct a suitable apparatus.
2. Investigate viable thin film deposition technologies and establish a procedure for deposition on a plastic scintillator substrate.
3. Quantify the mitigation of the radioxenon memory effect in plastic scintillator samples coated by techniques established in item 2.

Chapter 2: Theory

2.1 Radioxenon Production

There are a number of physical processes vital to production of radioxenon, whether the xenon is produced by activation in a reactor or as a fission product in a nuclear weapon detonation. One of these processes, and the one that defines radioactivity, is decay.

Unstable isotopes have a nuclear arrangement that is not sustainable indefinitely due to a deficit or excess of neutrons in the nucleus. This parent nucleus will go through a characteristic decay that will create a daughter nucleus. The time dependence of this decay is described by the half-life of the parent nucleus. The half-life, conventionally written as $\mathbf{T_{1/2}}$, is a physical property of each isotope that describes the time it takes for half of the nuclei of that isotope to decay. Half-lives can range from less than milliseconds for some isotopes to millions of years or more for others. It is useful to re-express the half-life in terms of the decay constant, denoted by $\boldsymbol{\lambda}$, where we define

$$\lambda = \frac{\ln 2}{T_{1/2}} \tag{2.1}$$

For an initial collection of $\mathbf{n_o}$ nuclei of an isotope with half-life $\mathbf{T_{1/2}}$, we can then write the number of nuclei as a function of time as

$$n(t) = n_o e^{-\lambda t} \tag{2.2}$$

where $\mathbf{t}$ is the time between measurement of $\mathbf{n_0}$ and $\mathbf{n(t)}$. Similarly, the activity of a sample of a single isotope can be written as

$$a(t) = a_o e^{-\lambda t} \tag{2.3}$$

where **a(t)** is the measured activity and $\mathbf{a_0}$ is the initial activity.

Every radioactive isotope has a set of possible daughter nuclei and, for each decay, the decay mode determines which daughter is produced. Although decay can occur with the emission of a neutron, by spontaneous fission, or a number of other processes, the most common decays occur with the emission of an alpha particle, a beta particle, or a gamma ray. Alpha emission is rare among isotopes lighter than lead, thus beta emission and gamma emission are the most significant processes in consideration of radioxenon decay [55].

Beta decay occurs when an unstable nucleus emits an electron or positron, conventionally known as a β^- particle or β^+ particle, respectively. The general equations for these decay modes are written as

$$^{A}_{Z}X \rightarrow {}^{A}_{Z-1}X + \beta^{+} + \upsilon_e \tag{2.4}$$

$$^{A}_{Z}X \rightarrow {}^{A}_{Z+1}X + \beta^{-} + \bar{\upsilon}_e \tag{2.5}$$

where **X** identifies the chemical symbol of the isotope, the superscript describes the number of nucleons in the atom and the subscript describes the number of protons. The emission of the beta particle distinguishes the decay as the β^+ mode or the β^- mode. The emission of the electron neutrino or antineutrino is necessary to conserve lepton number.

Nuclei can also decay by interacting with one of the innermost electrons in the atom in a process called electron capture. A neutron is formed from the

interaction of a proton and the captured electron, thus producing a daughter nucleus identical to that produced in β^+ decay. An X-ray is emitted in this process as an electron de-excites to the energy state previously held by the captured electron.

In many cases, the daughter product of a decay event is left in an excited nuclear state. Similar to the de-excitation of an electron and subsequent emission of an X-ray, nuclei can decay from excited states and emit a gamma ray. Often this decay happens quickly after the beta decay of the atom and the gamma emission is considered to be coincident with the initial decay. These gamma rays have characteristic energies that, if measured, can be used to identify the parent nucleus. However, it is possible for nuclei to remain in this excited state for some time after beta decay and the excited nucleus can be considered to be in a metastable state. These metastable states are denoted by the letter m following the mass number in nuclear notation, such as in ^{133m}Xe, and have characteristic gamma emissions [55].

In addition to simple emission of a gamma ray, these metastable states can decay to a stable nuclear state by emission of an orbital electron in a process called internal conversion. Unlike beta decay, this process does not change the number of neutrons or protons in a nucleus. A characteristic X-ray is emitted when the electron vacancy is filled. Both ^{131m}Xe and ^{133m}Xe decay by this process.

All of the processes discussed thus far are based solely on the properties of an individual nucleus and require no interaction with external particles or atoms. However, neutron interactions are relevant to radioxenon production via activation in a reactor and production in a nuclear weapon.

When a free neutron is incident on a nucleus, there are a number of interactions that can occur. The neutron can scatter elastically or inelastically, be captured with re-emission of a gamma ray, charged particle or another neutron, or it can induce fission in the nucleus. Each of these interactions occurs with some probability described by the cross-section of the interaction. Cross sections are given in units of barns, equivalent to 10^{-24} cm^2, and are dependent on the isotope involved in the interaction and the energy of the incident neutron. Of interest for xenon production are the processes of neutron capture and fission.

Neutron capture is generally the process by which activation is possible. When a neutron is incident on a nucleus, the nucleus can absorb the neutron according to the reaction

$$n + {}^{A}_{Z}X \rightarrow {}^{A+1}_{Z}X + \gamma \tag{2.6}$$

Activation is the production of an isotope by subjecting it to a neutron source in order to cause neutron capture events.

Table 2.1 Naturally occurring isotopes of xenon and their abundance.

Isotope	Abundance (%)
^{124}Xe	0.1
^{126}Xe	0.09
^{128}Xe	1.91
^{129}Xe	26.4
^{130}Xe	4.1
^{131}Xe	21.2
^{132}Xe	26.9
^{134}Xe	10.4
^{136}Xe	8.9

In many cases, including the activation of xenon for the purposes of this project, a stable isotope is activated to produce a radioactive isotope. Xenon has nine stable isotopes, listed in Table 2.1, subject to activation when natural xenon is irradiated in a reactor. The relative yield of the activated isotopes is dependent on many parameters: the natural abundances and cross section of each xenon isotope, the neutron energy profile of the irradiation facility, the half-lives of the various xenon isotopes, the irradiation time and the decay time. Calculations have been conducted to determine the expected yield for specific sets of parameters [56].

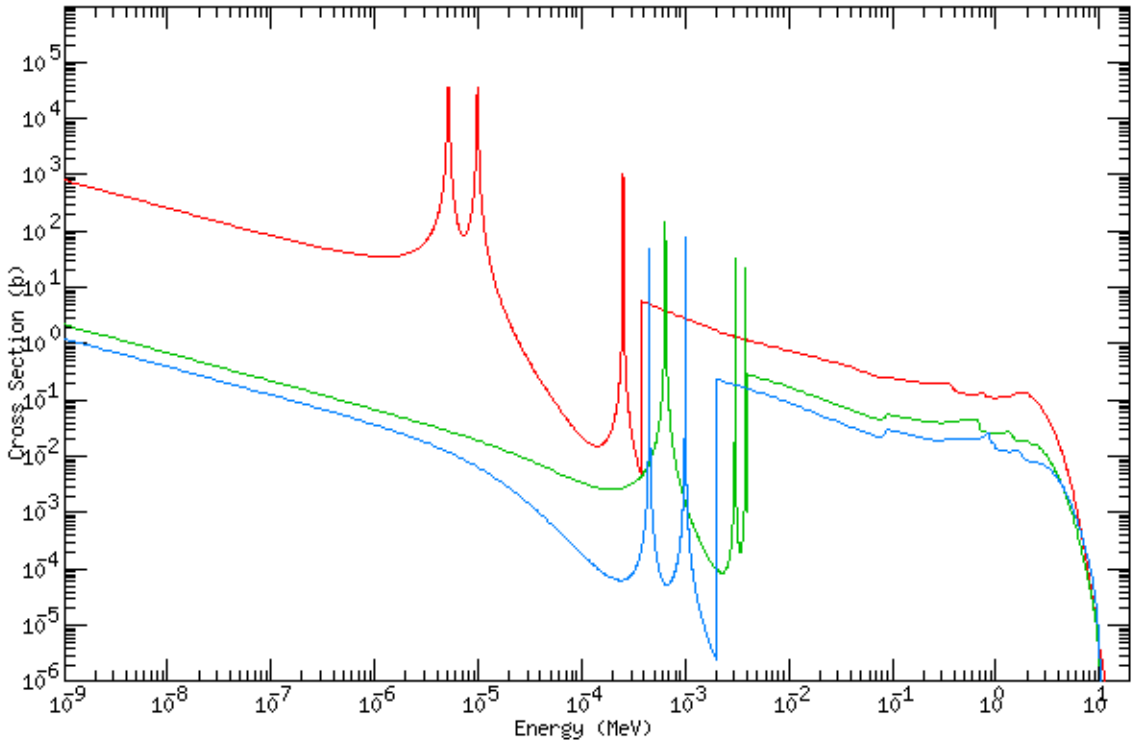

Figure 2.1 Neutron capture cross section as a function of neutron energy for ^{124}Xe, ^{132}Xe, ^{134}Xe in red, green, and blue, respectively [57].

The very high cross section resonance in the epithermal range for ^{124}Xe, as seen in Figure 2.1, leads to dominance of ^{125}Xe ($T_{1/2} = 16.9$h) in spectra collected within days of the irradiation. The long half-life of ^{133}Xe ($T_{1/2} = 5.243$d) allows that isotope to dominate spectra collected long after the irradiation. The relatively high cross section of ^{134}Xe and appreciable half-life of ^{135}Xe also leads to ^{135}Xe signals detectable in post-irradiation spectra. For the nominal parameters used for xenon activation in this project, ^{125}Xe, ^{133}Xe, and ^{135}Xe produce the dominant post-irradiation signals.

The other important neutron interaction for xenon production is that of fission. Although fission can happen spontaneously, as radioactive decay does, fission can also be induced from the interaction of a neutron and a fissionable nucleus. The fission process involves the absorption of a neutron by a large nucleus, the formation of an unstable nucleus, and the prompt fragmenting of the nucleus into two or more fission products. Each fission event has a probability of releasing a number of free neutrons that can then induce further fission events. This chain reaction, when self-sustaining, is the basis for heat production in nuclear power plants and energy release in nuclear weapons.

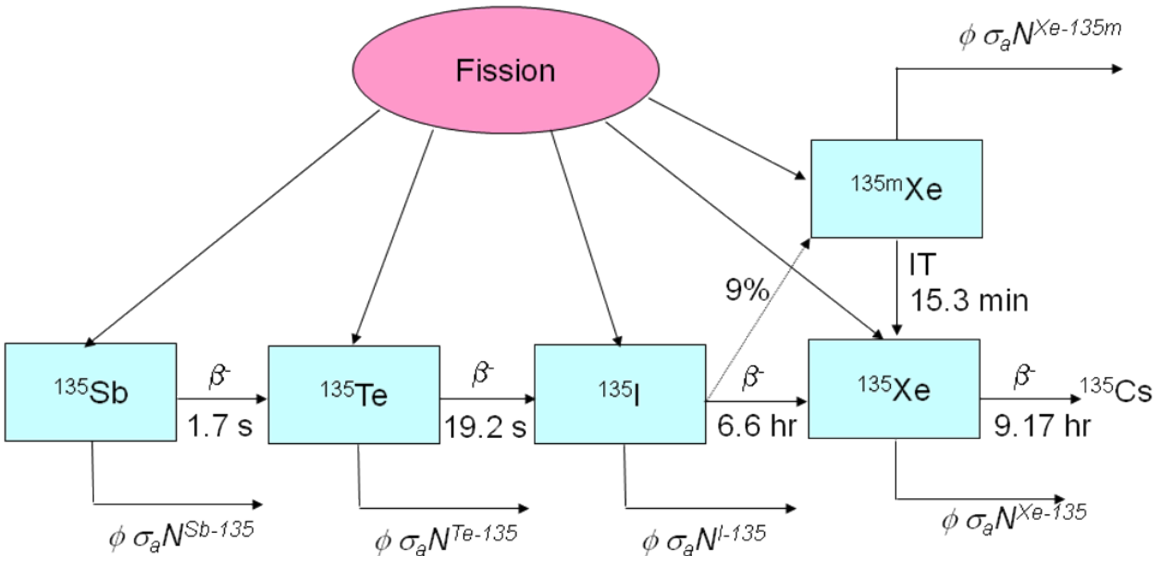

Figure 2.2 Pathways for the production of ^{135}Xe from a fission event [58].

The yield of a fission product in a weapons detonation or nuclear power reactor is determined by a number of processes. Each fissionable isotope has a characteristic probability distribution for production of each fission product. The independent yield, or initial yield, is dependent on this probability distribution, as well as the energy of the incident neutron. The cumulative yield of a specific fission product is determined by the independent yield and the decay chain leading to the fission product. These dependencies are illustrated in Figure 2.2.

2.2 Radioxenon Monitoring

Xenon becomes a relevant element for weapons detonations and nuclear reactors because it is produced in relatively high quantities in fission events, as indicated by Figure 2.3. Nuclear reactors, reprocessing facilities, medical isotope production facilities, and nuclear weapons detonations have been identified as the major sources of radioxenon [7]. In the course of atmospheric monitoring,

emission from all of these sources will be detected. It then becomes important to develop means to distinguish an explosion source from the other three sources.

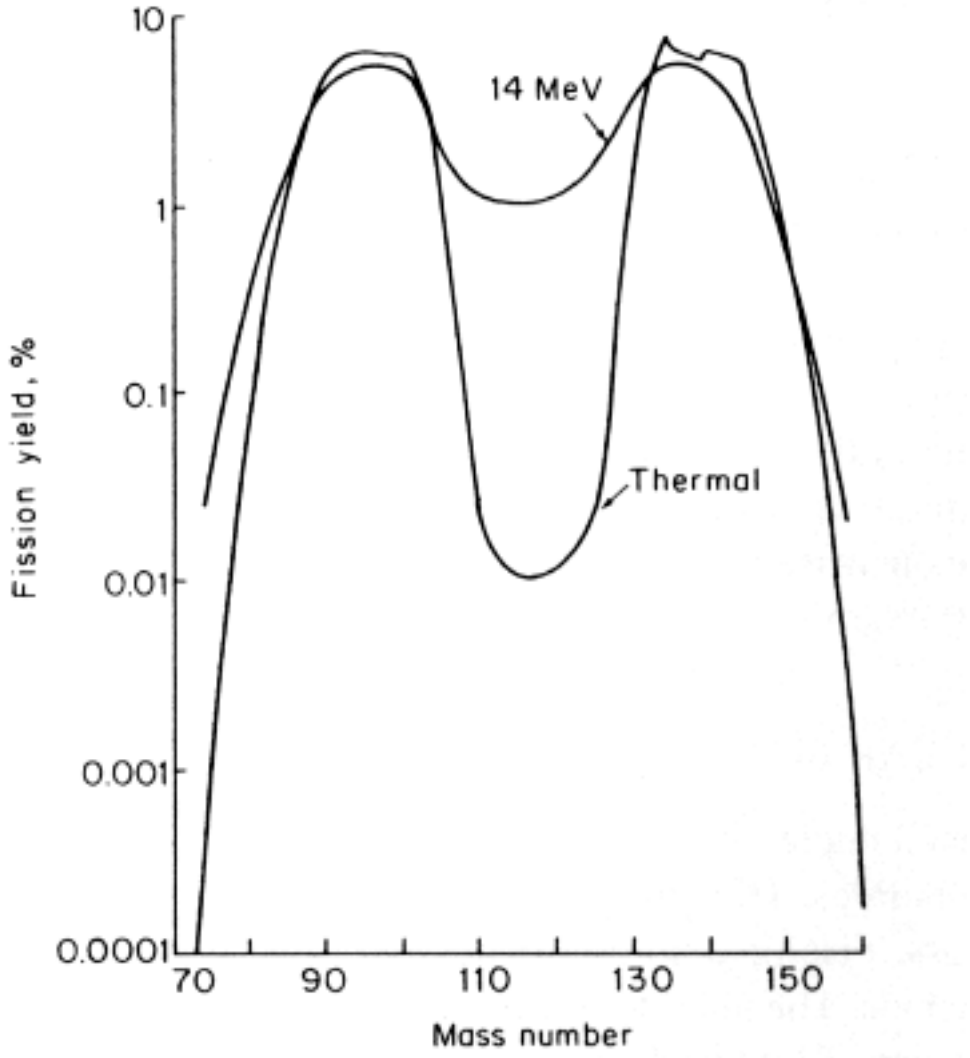

Figure 2.3 Fission product spectrum for ^{235}U. For xenon isotopes of interest, mass numbers range from 131 to 135 [64].

Although many xenon isotopes are part of the fission product spectrum for fissile materials, some isotopes have half-lives on the order of seconds (^{139}Xe

and higher and many of the metastable states) [57] and will not be detectable by remote monitoring stations. Other xenon isotopes are too low yield to be detected. INGE stations monitor four xenon isotopes: ^{131m}Xe, ^{133m}Xe, ^{133}Xe, and ^{135}Xe. The half-lives and respective yields for these isotopes are given on Table 2.2.

Table 2.2 Half-life and yield per 100 fissions for the four xenon isotopes monitored in the IMS. Yield is given for fast neutrons [59].

Isotope	**Half-Life**	**Ind. Yield**	**Cum. Yield**
^{131m}Xe	11.9 d	2.41E-07	0.0451
^{133m}Xe	2.1 d	4.23E-03	0.192
^{133}Xe	5.2 d	1.46E-03	6.72
^{135}Xe	9.1 h	0.12	6.6

The expected ratio of these four isotopes with respect to each other will vary based on the processes by which they are produced [56], thus they will vary between sources. Of primary significance is the irradiation time difference between the sources [57]. Irradiations at medical isotope facilities are on the order of days and irradiation at power reactors can last for months, however the effective irradiation time in a nuclear weapon detonation is much less than a second. This difference in irradiation time, among other, less significant effects, can lead to order of magnitude or larger differences between the expected ratios from an explosion and the other three sources [56]. The measurement of these ratios then makes the radioxenon monitoring process a viable option for verification of a nuclear explosion.

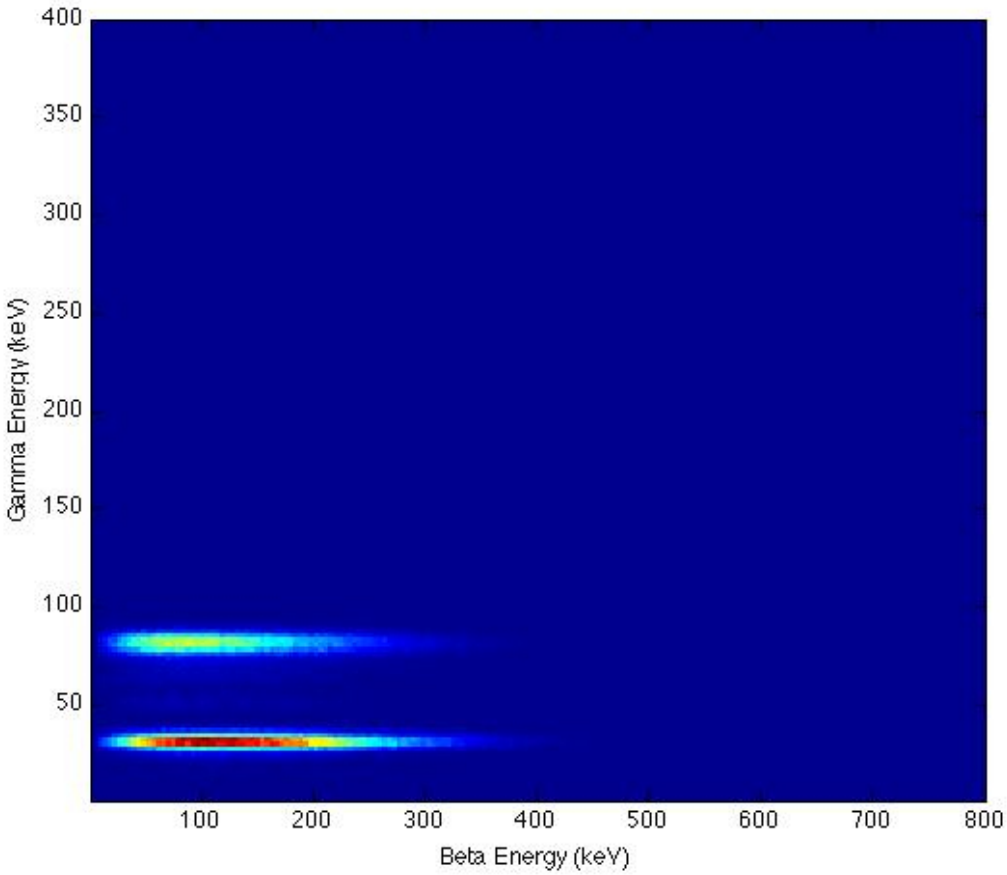

Figure 2.5 Beta-gamma coincidence spectrum of ^{133}Xe [56].

As mentioned in the discussion of radioactive decay in this chapter, the decay of excited nuclear states often happens immediately following the emission of a beta particle. If the half-life of the excited nuclear state is sufficiently small compared to the half-life of the beta decay mode, it is possible to associate the detection of the gamma ray with the detection of the beta particle. This counting technique is known as beta-gamma coincidence and is the basis for radioxenon measurements in the ARIX, ARSA, and SAUNA monitoring stations. The advantage of coincidence counting is the substantial reduction of

background in which many events will not occur simultaneously. Beta-gamma counting, in the context of the aforementioned radioxenon monitoring stations, relies on two fundamental detection technologies: NaI crystals for gamma ray detection and plastic scintillator for beta detection. A beta-gamma coincidence spectrum of ^{133}Xe is given in Figure 2.5.

Sodium iodide (NaI) crystal detectors are inorganic scintillators used in gamma spectroscopy. If an incident gamma ray deposits its energy into the crystal, an electron can be elevated into the conduction band of the crystal's energy band structure. In a normal material, this free electron would de-excite with the emission of a photon with energy too high to be collected in a photomultiplier tube. However, if the crystal is doped in such a way that there are available energy states within the forbidden gap, the de-excitation energy of the conduction electron can be conserved by emission of a series of photons in the visible spectrum [60]. These photons can then be collected by a photomultiplier to be read as an electrical signal. In the case of a NaI detector, the dopant is commonly thallium, leading to the convention NaI(Tl). The high light yield and adaptability of NaI crystal makes it a suitable material for gamma detection in radioxenon monitoring stations.

Beta particle detection is achieved by a process similar to gamma detection in a NaI(Tl) crystal. Organic scintillator fluoresces by the same basic mechanism as inorganic scintillator, however absorption of incident energy leads to the excitation of individual molecules rather than atoms in a crystal structure [60]. The spacing between energy states in a scintillating molecule is generally between 1 and 4 eV, thus de-excitation of the molecule produces visible spectrum photons

that can be collected in a photomultiplier. Anthracene is one of the most common organic scintillators, and it is used in all the radioxenon monitoring station designs discussed in this paper [61].

Just as a NaI(Tl) detector is designed with the maximum gamma energy absorption in mind, a scintillator for beta detection must be designed to maximize the efficient absorption of incident electron energy.

The charge and low mass of the electron prevent it from being highly penetrating when emitted from a decay event. The range of a beta particle in an absorbing medium is described by a system of empirical formulas, given as equations (2.7) and (2.8) [55],

$$R_{\max}\rho = 0.412 E_{\max}^{(1.265-0.0954\ln E_{\max})}, \quad E_{\max} < 2.5 MeV \tag{2.7}$$

$$R_{\max}\rho = 0.530 E_{\max} - 0.106, \qquad E_{\max} > 2.5 MeV \tag{2.8}$$

where $\mathbf{R_{max}}$ is the range of the beta particle, $\boldsymbol{\rho}$ is the density of the absorbing material, and $\mathbf{E_{max}}$ is the maximum energy of the beta particle energy distribution in MeV. Beta particle energies for xenon decay are below 2.5 MeV, thus calculations relevant to xenon will use equation (2.7). The range for beta particles in PVT, calculated with this equation, is given in Figure 2.6.

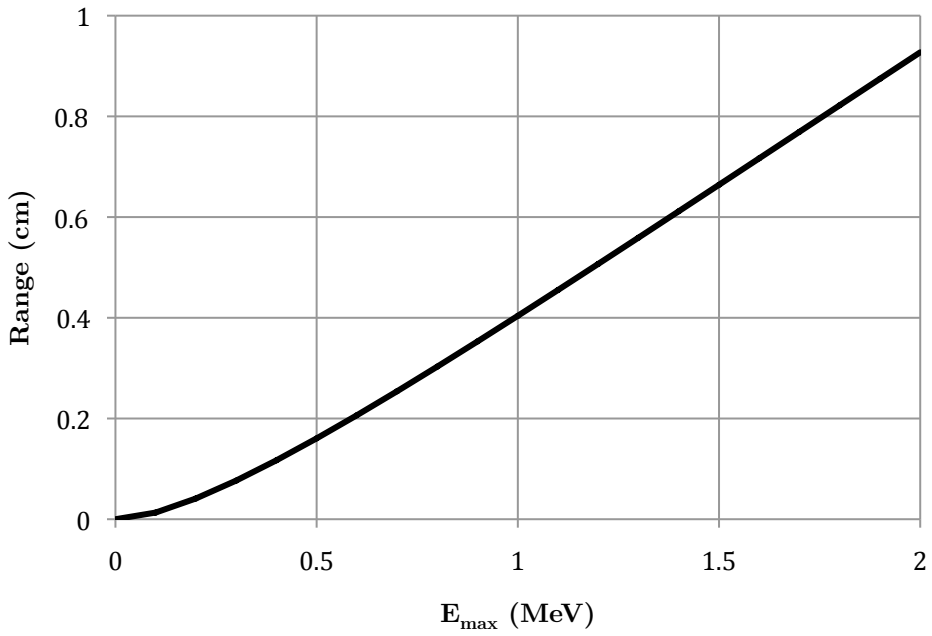

Figure 2.6 Beta particle range in polyvinyltoluene based on equation (2.7).

An additional, and vital, consideration for beta detection is the geometry of the coincidence detector system. The radioxenon is entirely contained in the plastic scintillator cell, which is entirely contained in the NaI(Tl) crystal, as indicated in Figure 2.7, thus the plastic scintillator must have minimal interactions with gamma rays so as not to impact the efficiency of the gamma counting system.

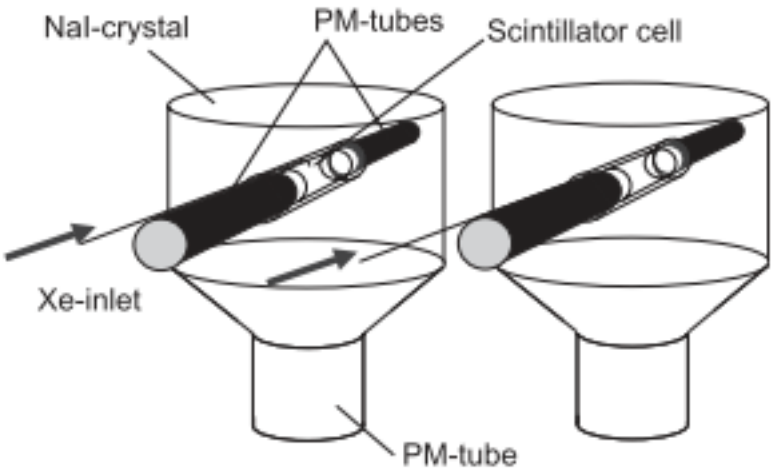

Figure 2.7 Detector arrangement in the SAUNA [12].

High photon transparency, even at low energies, and the ease of manufacturing plastic in various geometries makes plastic an apt material for beta measurement. Organic scintillator can be polymerized to produce a plastic scintillator that satisfies the need for high beta efficiency and extremely low gamma efficiency. The material used for beta counting in the radioxenon stations discussed elsewhere in the thesis is polyvinyltoluene doped with anthracene [61].

2.3 Inert Gas Diffusion

The change in concentration of some substance as a function of position is given by Fick's Law:

$$J = -D\nabla n \tag{2.9}$$

where **J** is the flux of the substance, **D** is the diffusion coefficient of the substance in the medium, and **n** is the concentration of the substance. It is important to note that Fick's Law describes the flux as a function of position

and is time independent. The concentration is described as a function of time by Fick's Second Law

$$\frac{\partial n}{\partial t} = D\nabla^2 n \tag{2.10}$$

For radioactive species, the decrease in concentration as a result of radioactive decay is described by

$$\frac{\partial n}{\partial t} = -\lambda n \tag{2.11}$$

which, when solved, gives equation (2.2). The concentration of a radioactive material undergoing diffusion is then most generally described by

$$\frac{\partial n}{\partial t} = D\nabla^2 n - \lambda n \tag{2.12}$$

When the del operator is expressed explicitly in Cartesian coordinates, equation (2.12) becomes

$$\frac{\partial n}{\partial t} = D\left(\frac{\partial^2 n}{\partial x^2} + \frac{\partial^2 n}{\partial y^2} + \frac{\partial^2 n}{\partial z^2}\right) - \lambda n \tag{2.13}$$

For the geometry considered in this project, we can estimate the thickness of the sample to be small relative to the other dimensions such that we estimate thin plate geometry and simplify equation (2.13) to

$$\frac{\partial n}{\partial t} = D\frac{\partial^2 n}{\partial x^2} - \lambda n \tag{2.14}$$

where the x-direction is defined by the axis perpendicular to the surface of the sample exposed to xenon. When applied to this project's experimental setup, a thin plate of plastic of thickness **L** exposed to a concentration **c** of radioxenon for time **T**, then measured for activity some time after the exposure, (2.14) has to be solved as two initial-boundary value problems. The first set of initial-boundary conditions describes the concentration of xenon in the sample during the exposure. The second set describes the concentration of xenon in the sample after exposure. The primary difference between these two sets of conditions is the presence of a time-dependent concentration of xenon outside the source in the first set that is absent for the second set.

The first set of initial-boundary conditions can be solved [48] to give

$$n(x,t) = \frac{4Dc}{L} \sum_{k=0}^{\infty} \frac{\frac{(2k+1)\pi}{L}}{\lambda_{2k+1} - \lambda} \left(e^{-\lambda t} - e^{-\lambda_{2k+1} t} \right) \sin\left(\frac{(2k+1)\pi}{L} x \right) \qquad (2.15)$$

while the second set of conditions is solved by

$$n(x,t) = \frac{4Dc}{L} \sum_{k=0}^{\infty} \frac{\frac{(2k+1)\pi}{L}}{\lambda_{2k+1} - \lambda} \left(e^{-\lambda T} - e^{-\lambda_{2k+1} T} \right) e^{-\lambda_{2k+1} t} \cdot \sin\left(\frac{(2k+1)\pi}{L} x \right) \qquad (2.16)$$

where

$$\lambda_n = \lambda + \left(\frac{n\pi}{L} \right)^2 D \qquad (2.17)$$

Equation 2.16 can then be integrated over the volume of the thin plastic plate to give the total activity as a function of time as

$$a(t) = \frac{8\lambda^2 ScL_D^2}{L} \sum_{k=0}^{\infty} \frac{e^{-\lambda T} - e^{-\lambda_{2k+1} T}}{\lambda_{2k+1} - \lambda} e^{-\lambda_{2k+1} t} \tag{2.18}$$

where **S** is the surface area of the plastic and $\mathbf{L_D}$ is the diffusion length of xenon in the plastic, defined as $\sqrt{D/\lambda}$. Further simplification of (2.18) requires the empirical calculation of L_D. Measurements of the activity in the plastic at large values of **t** can be used to calculate λ_1, from which L_D can be determined using (2.17).

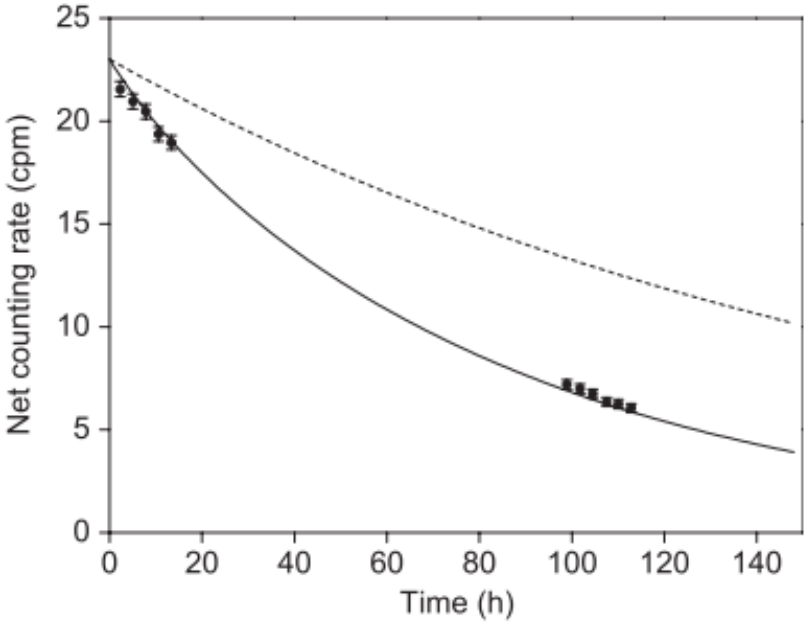

Figure 2.8 Desorption of ^{133}Xe in polycarbonate. The points indicate empirical data, the solid line represents theoretical values from equation (2.18), the dashed line represents radioactive decay [48].

Much of this mathematical treatment follows the theory presented in the reference by Pressyanov [48]. Beyond this simplification, this reference empirically calculated the diffusion length for xenon in the material and geometry relevant

to their experiment then fit equation (2.18) to experimental data using a scale factor. This fitting equation agreed with empirical results that showed, for a 0.3 mm polycarbonate plate after a 383 hour ^{133}Xe sorption period, desorption of 80% of the original ^{133}Xe activity over roughly 100 hours as indicated in Figure 2.8.

2.4 Plasma Enhanced Chemical Vapor Deposition

There are a number of designs for PECVD reactors and, in most cases, the design determines the kinetics and chemistry of the reaction and thin film deposition. Deposition in this project was conducted on a PlasmaTherm 790 parallel plate reactor and the kinetics and chemistry for this reactor architecture are discussed below.

The bottom plate of the parallel plate electrode also serves as the substrate platform. Temperatures given for PECVD processes indicate the temperature to which this platform is heated, though it is commonly assumed that this is the substrate temperature as well. An RF generator drives a 13.56 MHz frequency signal across the plates. The high electric field produced by the RF produces a number of species within the newly formed plasma [34].

Charged particles both induce chemical reactivity in the plasma and are the basis for the formation of the thin film. Negatively charged free electrons within the plasma collide with other species, fragmenting the original reactant gas molecule or exciting an atom to increase the likelihood of a chemical interaction. Additionally, the high electron mobility of the plasma leaves the substrate at negative potential with respect to the plasma. Thus positively

charged ions in the plasma will bombard the surface of the substrate and form the thin film.

Beyond charged particle interactions, radicals within the plasma are formed as molecules fragment and chemical reactions create new species. Continuous reactions between radicals can form the desired thin film composition, however in many cases these radicals are deposited onto the surface of the substrate before the desired composition is produced, thus forming a source of impurity in the film.

For the formation of SiO_2 films, the reactant gases are silane and nitrous oxide. The fundamental reaction for the production of SiO_2 with these reagents is

$$SiH_4 + 2N_2O \rightarrow SiO_2 + 2H_2 + 2N_2 \tag{2.19}$$

However species such as N-H, Si-H, Si-O-H are also produced as a result of other reactions [30]. Dilution of the reagent gases with a carrier such as He or N_2 can reduce the production of these species and thus reduce the impurities in the thin film.

Chapter 3: Experiment

3.1 Xenon Activation

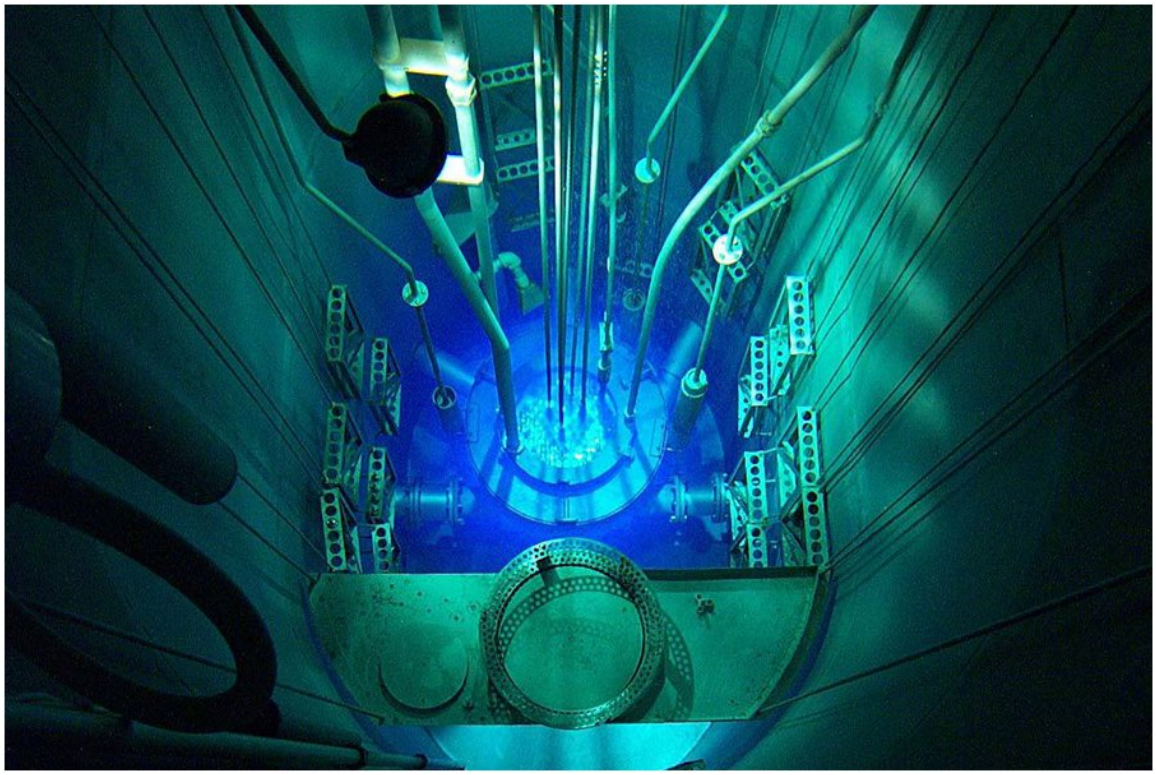

Figure 3.1 Core of the NETL TRIGA reactor.

Xenon production for this experiment took place at the University of Texas TRIGA Mark II reactor at the Nuclear Engineering Teaching Laboratory (NETL), pictured in Figure 3.1. The 1.1 MW NETL-TRIGA reactor facilities include in-core and ex-core irradiation locations, tangential and perpendicular beam ports, a rotating specimen rack (RSR), and pneumatic sample transfer systems. The facility of interest for this work was the tri-element (3L) facility, which is an in-core irradiation site and is pictured in Figure 3.2.

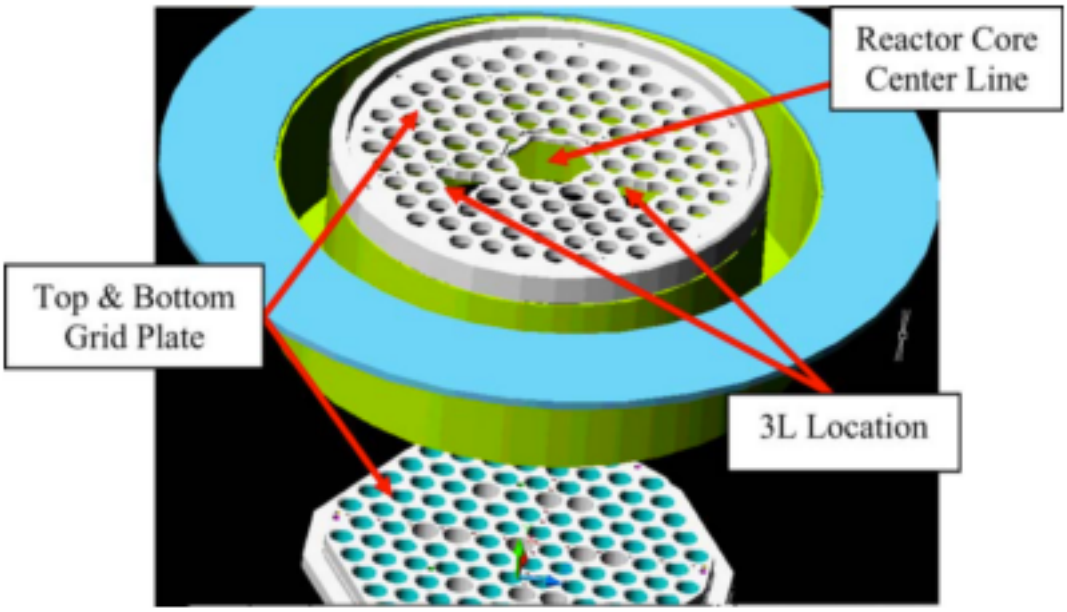

Figure 3.2 Exploded view of 3L facilities in the NETL TRIGA core [63].

At the 3L site three fuel pin receptacles are cut out to allow the insertion of a support structure for an aluminum sample vessel. The schematics of the vessel are given in Figure 3.3. The vessel is a hollow outer cylinder with outer diameter of 1.875" and a hollow inner cylinder with inner diameter of 1.527". Between the cylinders is a 0.04" sheet of either lead or cadmium. The cylinders are 48.125" long with a plug welded to the bottom and a removable threaded cap on top. Pressure relief valves built into the cap maintain a constant pressure within the vessel during irradiation. The cap, plug, and cylinders were machined from 6061 aluminum.

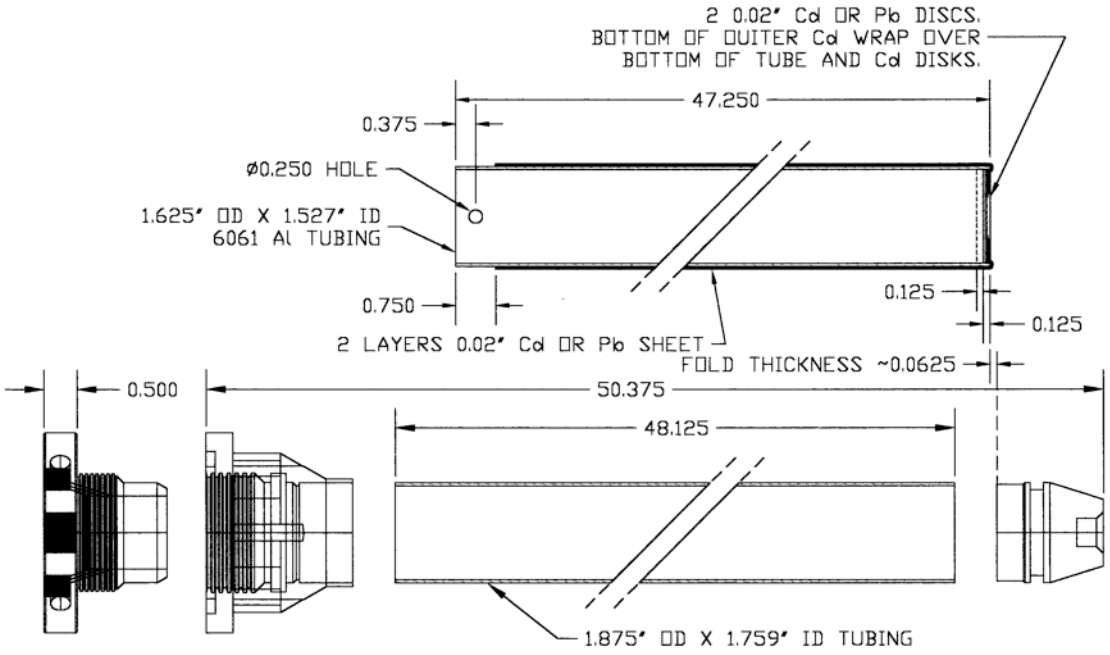

Figure 3.3 3L sample vessel schematic.

The lead lining serves to counterweight the sample vessel against buoyancy while the cadmium lining serves to shield the sample chamber within the vessel from thermal neutrons. Thus the lead lined vessel is used as a full spectrum facility and the cadmium lined vessel is used as an epithermal irradiation facility, where the cadmium cutoff, or the energy below which a majority of neutrons are absorbed, is roughly 0.5 eV [60].

In order to produce radioxenon, purified xenon at natural isotopic levels was transferred to a perfluoroalkoxy (PFA) valve, pictured in Figure 3.4, which was then inserted into the Cd-lined sample vessel in the 3L facility. The gas is contained within the 2 mL chamber in the rotating portion of the valve, as well as the endcap.

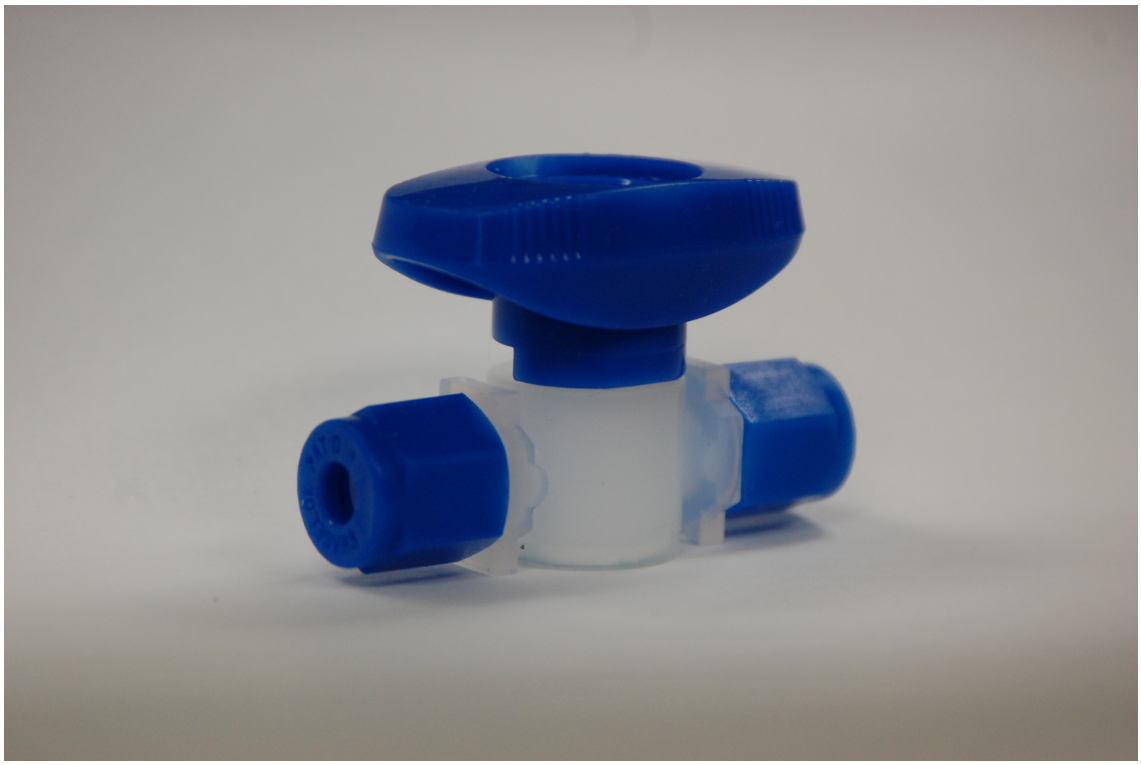

Figure 3.4 PFA valve used for natural xenon irradiation in NETL-TRIGA reactor.

Transfer of the natural xenon from a compressed gas cylinder to the PFA valve was accomplished using the gas transfer manifold, developed at Pacific Northwest National Laboratory (PNNL) and pictured in Figure 3.5. A two-stage CGA-580 regulator was attached to the compressed gas cylinder then connected to the manifold. The PFA valve was set to the open position and connected to the manifold. The entire manifold, including the valve and tubing to the regulator, was evacuated then flushed with N_2. This "pump and flush" process was repeated to ensure minimal contamination of the xenon within the valve. Following the final evacuation of the entire system, the manifold was set up to allow flow from the regulator to the valve. The compressed gas cylinder was

opened, as well as the needle valve between the regulator and manifold. The regulator was used to bring the pressure of the entire system to roughly 1.3 bar, at which point the PFA valve was isolated from the manifold, closed, then removed from the manifold. The operation of the relevant valves on the transfer manifold is shown for the entire process in Appendix A.

After irradiation, the PFA valve was counted for 20 minutes to verify the presence of ^{125}Xe, ^{133}Xe, and ^{135}Xe.

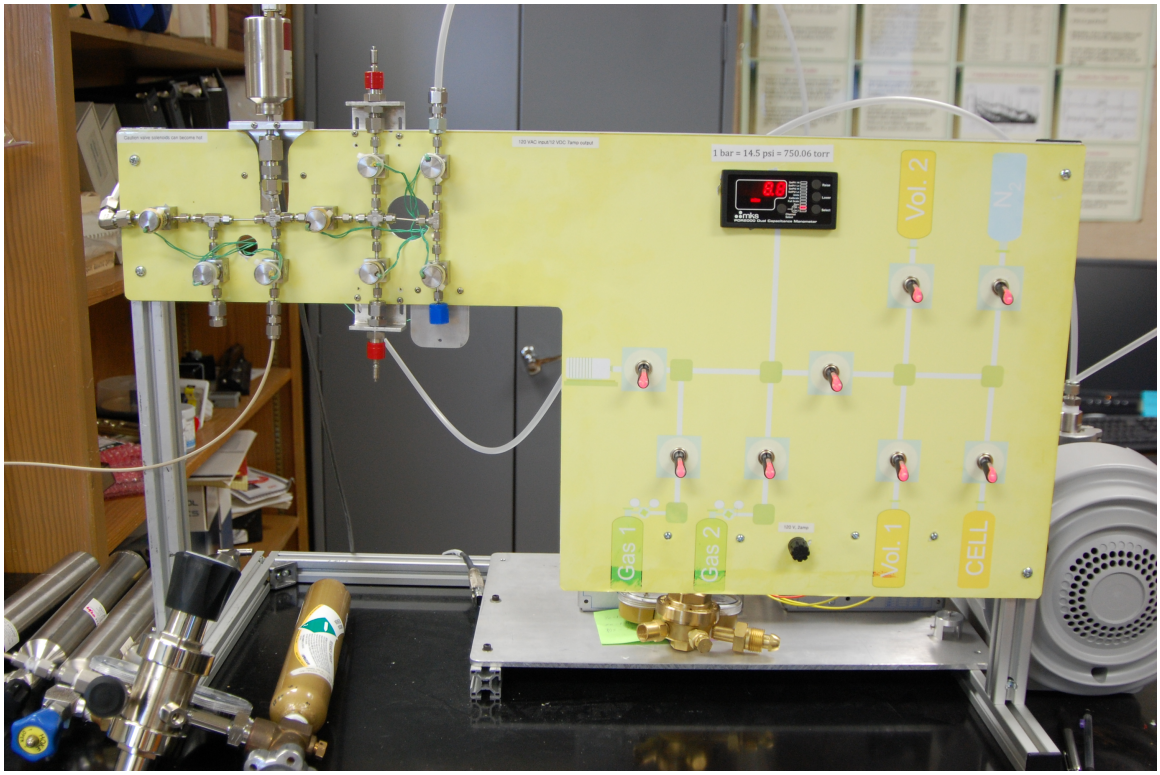

Figure 3.5 Gas transfer manifold used for preparation of xenon samples and the evacuation of exposure manifold.

3.2 Sample Preparation and Exposure

In order to expose the BC-404 samples to the radioxenon contained in the PFA valve, the samples were affixed to stainless steel hex nuts that were then attached to the exposure manifold. Optical cement from Eljen Technology (EJ-500) and Saint Gobain (BC-600) was used to adhere the plastic scintillator to the stainless steel. These products were chosen because of their viability with both stainless steel and plastic, as well as their resistance to outgassing. Both products came with resin and hardener. The epoxy was created by mixing 4 parts by weight resin with 1 part by weight hardener in a plastic petri dish. The mixture was left to settle for 30 minutes to allow bubbles to rise to the surface then was applied to the contact surface of the hex nut. The BC-404 sample was pressed onto the contact surface and centered. Care was taken to minimize the coverage of the cement on the inner surface area of the plastic so as not to change the effective exposure area. All samples were left to dry 48 hours before use.

Two BC-404 geometries were tested: a cylindrical geometry of 0.1" height and 0.6" diameter as well as a 1" x 1" x 0.1" geometry. The cylindrical, or "endcap" geometry was cemented to a 0.5" hex nut that provided 0.196 in^2 of exposed surface area. The 1" x 1" x 0.1", or "square", sample was cemented to a 0.75" diameter hex nut, pictured in Figure 3.6, that provided 0.442 in^2 of exposed surface area. The use of the larger nut required a 0.5" to 0.75" stainless steel adapter.

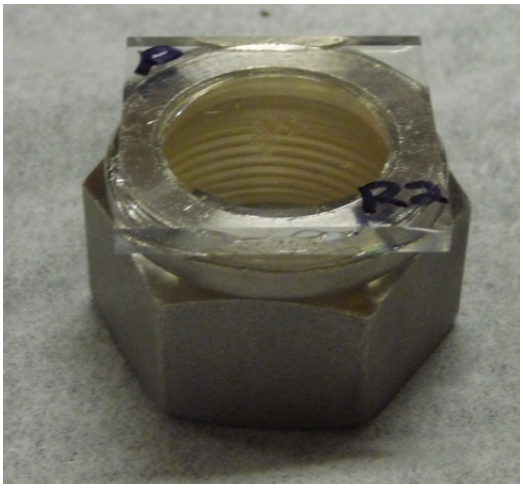

Figure 3.6 Square geometry sample cemented to a 0.75" stainless steel hex nut.

To avoid the introduction of radioactive gas to the transfer manifold, a separate exposure manifold was constructed. The exposure manifold, pictured in Figure 3.7, consisted of fittings to connect the exposure manifold to the transfer manifold and the PFA valve, as well as a mixing chamber and attachments for two testing chambers. Quarter turn valves were installed to allow for isolation of each test chamber, the manifold connection and the PFA valve connection. A schematic of the exposure manifold can be found in Appendix B.

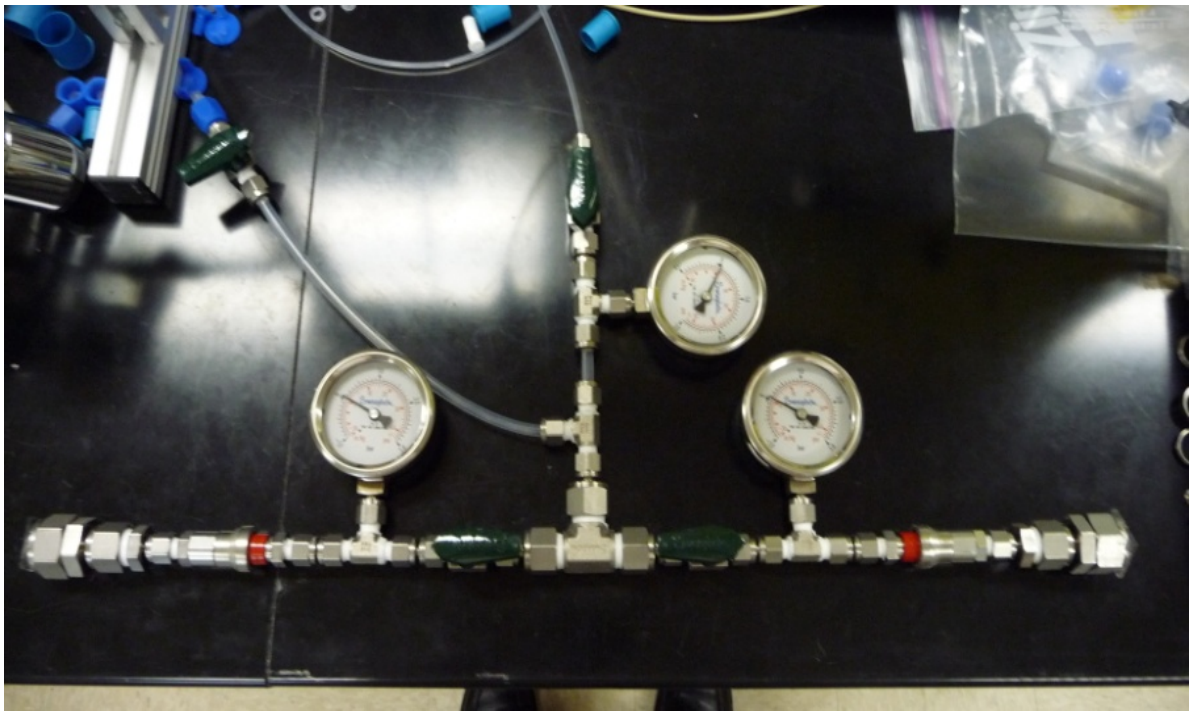

Figure 3.7 Xenon exposure manifold.

After the BC-404 samples were affixed to the stainless steel hex caps, the caps were tightened to the test chambers. Each test chamber was evacuated on the transfer manifold, then isolated from the vacuum and monitored to ensure the epoxy seal held vacuum. The test chambers were attached to the exposure manifold then, with the PFA valve connection isolated, the entire exposure manifold was connected to the transfer manifold and evacuated. The exposure manifold was subsequently flushed with N_2 then evacuated again. Several "pump and flush" cycles were conducted to remove contaminants from the exposure manifold. After the final evacuation the exposure manifold was backfilled with N_2 to 0.9 bar, then the transfer manifold connection was isolated and the exposure manifold was disconnected from the transfer manifold.

With both test chamber valves open, the transfer manifold attachment valve closed and the PFA valve attachment closed, the PFA valve containing the radioxenon was threaded onto the exposure manifold. The quarter turn valve on the exposure manifold was opened and the gauges on the manifold were monitored to ensure the system remained sealed while attached to the PFA valve. Finally, the PFA valve was opened to release the radioxenon into the manifold. Exposures ranged from 18 to 24 hours, after which the PFA valve attachment was closed, both test chambers were disconnected from the exposure manifold, and the hex nuts with the BC-404 samples were removed from the test chamber for counting.

The operation of the relevant valves on the exposure manifold is detailed in Appendix B.

3.3 Activity Measurement

Normal counting techniques would allow for serial counting of two samples. Post-processing of the spectra with decay and count time corrections would normalize the second count to the first, and activity levels could be compared. However, for the purposes of this experiment, the activity in the BC-404 sample as a function of time is determined both by the decay of xenon isotopes and the diffusion of the gas in the scintillator. In the absence of a quantitative model of xenon diffusion in polyvinyltoluene, counting must be done in parallel to eliminate diffusion as a parameter.

The intricacy introduced by simultaneous counting on different detectors is that of relative efficiency. With the intention of comparing data collected on

different detectors, we must determine the value of a count on one detector relative to the other. Discrepancies in counting geometry, absolute efficiency, and electronic instrumentation can account for these differences between detectors.

The Eckert & Ziegler Analytics Model 7603 mixed gamma emitter liquid check source was used in order to produce a relative efficiency curve as a function of gamma energy. The initial check source was 19 mL of the 4M HCl. This liquid was counted in a 2" diameter plastic petri dish. In order to better replicate the geometries of the BC-404 samples, two new check sources were produced. Whatman #1 filter paper was cut into 1" squares, then 80 μL of the 4M HCl mixed gamma source was deposited onto the filter paper and the filter paper was left to dry. Twenty of these dried 1" squares were stacked and sealed in plastic wrap. Final dimensions of the check source were 1" x 1" x 0.16" with the mixed gamma source distributed throughout each layer of filter paper.

A similar procedure was followed to replicate the endcap sample geometry. Whatman #4 filter paper was cut into identical 0.5" squares then 20 μL of the 4M HCl was deposited onto each square. After drying, 20 squares were stacked and sealed. Final dimensions of the source were 0.5" x 0.5" x 0.15" with the multigamma emitter distributed in the layers of the filter paper. These check sources were counted on each detector used for sample counting.

3.4 Plasma Enhanced Chemical Vapor Deposition

Thin film deposition and characterization was conducted at the University of Texas Microelectronics Research Center (MRC). The MRC has facilities for chemical vapor deposition, reactive ion etching, lithography, various metrology

techniques, and chemical processing. The PlasmaTherm RIE/PECVD #1, pictured in Figure 3.8, was used for PECVD deposition in this experiment.

Figure 3.8 PlasmaTherm parallel plate PECVD reactor.

All BC-404 samples put into the PECVD reactor were placed in a Pyrex petri dish to protect from contaminants on the reactor place surface as well as to serve as a container in the case of the BC-404 melting. The bottom of each sample was marked to distinguish between the side sitting on the petri dish and the side fully exposed to the reactor.

SiO_2 deposition was conducted at 800 mTorr and 100W of RF power. The temperature of the reactor was maintained at 60C.

Deposition in the PlasmaTherm was done in a number of steps. First, the reactor was initialized to the preset temperature and pressure for the deposition. Then the reactor was flushed with N_2 for 1 minute at 500 mTorr. Following the flush, the reactor was evacuated for 2 minutes. The reagent gases were then pumped into the reactor for 1 minute at 800 mTorr, followed by application of the RF power at 100W to induce the plasma in the reactor. The deposition times listed in the results section of this thesis describe the time that this RF power source was on. The flow rates for both steps requiring gas reagents were 160 sccm N_20 and 35 sccm SiH_4. At the conclusion of the plasma step, the reactor was again evacuated for 2 minutes then flushed with N_2 for 1 minute. The coated samples were retrieved from the reactor after it was pumped back to atmospheric pressure.

A list of PECVD parameters for each step is given in Appendix C.

3.5 Thin Film Characterization

Although plasma enhanced chemical vapor deposition can be conducted at low temperatures in silicon wafer applications, the temperatures required for deposition on plastic are sufficiently lower to suspect that deposition may be much different than at high temperatures on silicon. It then becomes important to do in situ characterization of the SiO_2 film, as opposed to characterization of SiO_2 on a proxy substrate. Two analytical techniques were employed for this characterization.

3.5.1 Neutron Activation Analysis

Neutron activation analysis was conducted at the NETL-TRIGA reactor to determine the deposition rate of the SiO_2. Two square geometry BC-404 samples were cut in half to produce four 1" x 0.5" samples. Two of these samples were covered with Kapton tape on all but one face, leaving the exposed surface area as 0.5 in^2. These two samples were simultaneously coated by PECVD for 6 minutes following the procedure from Section 3.4. Additionally, a silicon standard was created by depositing 0.03 mL of Inorganic Ventures CGSi10-1 silicon standard onto a 1" x 0.5" piece of Whatman #2 filter paper. This geometry was chosen to replicate that of the BC-404 samples. Each sample (the silicon standard on filter paper, two blank BC-404 samples and two SiO_2 coated BC-404 samples) was heat sealed in a 2.15" height by 0.65" diameter plastic vial. Each vial was placed in the NETL pneumatic sample system then irradiated in the NETL-TRIGA for 300 seconds. When the sample returned from the pneumatic system, it was placed on an HPGe detector to determine the count rate. The count rate was then used to determine the coating thickness by calculating the total mass of silicon on the sample and accounting for the known surface area that was coated.

3.5.2 Contact Profilometry

Contact profilometry is a technique similar to atomic force microscopy. In both analytical methods, a stylus is dragged across a surface and the variations of the force on the stylus are measured as variations in the height of the sample.

Profilometry data is given as a plot of stylus deflection as a function of horizontal position.

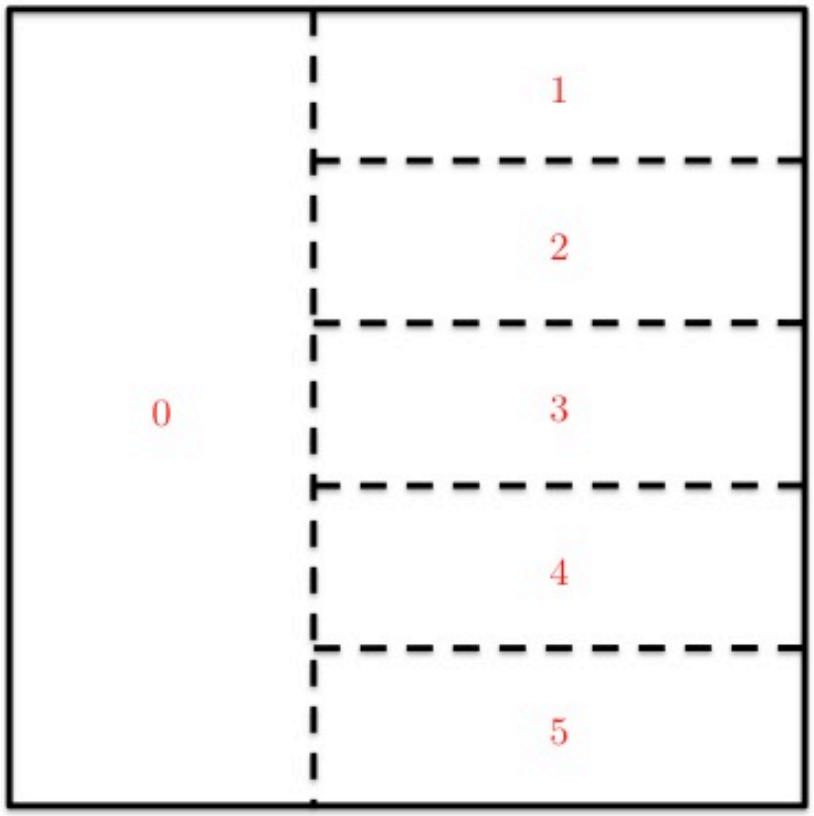

Figure 3.9 Deposition regions for characterization using profilometry.

In order to determine the deposition rate on the BC-404 using profilometry, a standard sample was created using the "square" geometry described in Section 3.2. This sample was coated according to the procedure described in Section 3.4, however the procedure was repeated with the uncovered surface area of the sample increasing with each iteration. The upper surface of the sample was considered as six regions, illustrated in Figure 3.9. Region 0 was first taped as a reference region. Then regions 1 to 4 were covered, in order, with

overlapping tape. Region 5 was left uncovered. With only region 5 uncovered, the sample was exposed for 3 minutes in the PECVD reactor. The sample was taken from the PECVD reactor then the tape on region 4 was removed. The sample was exposed for 3 minutes with regions 4 and 5 uncovered. The sample was again taken from the PECVD reactor and the tape from region 3 was removed. This procedure was repeated until region 1 was uncovered and exposed for 3 minutes. Region 0 was never exposed in the PECVD reactor.

Ultimately, the standard sample produced had five deposition regions: region 1 with a 3 minute exposure, region 2 with a 6 minute exposure, region 3 with 9 minute exposure, region 4 with a 12 minute exposure and region 5 with a 15 minute exposure. The profilometer was then scanned across the boundary between region 0 and each of the exposed regions to determine the step height and thus the thickness of the SiO_2 film for each exposure time.

Chapter 4: Results

4.1 Exposure Manifold

As part of the verification of the integrity of the exposure manifold, measurements of the leakage rate out of the manifold were planned. Evacuation of the manifold followed by measurements of the pressure in the manifold as a function of time would indicate whether there was considerable leakage that would lead to the venting of xenon during exposure. However no discernable change in pressure was seen in the manifold for measurements over a 72 hour period. Similarly, no measureable pressure change was seen over a 72 hour period for the manifold backfilled with N_2 to pressure of 0.9 bar, which replicates the state of the manifold during exposure. Exposure times were 18 +/- 2 hours, thus the performance of the manifold was deemed satisfactory. This leakage check was conducted intermittently throughout the course of the project to ensure no adjustments needed to be made.

4.2 Thin Film Characterization

Measurements of the SiO_2 deposition rate were conducted on the Alphastep Tencor profilometer as outlined in Chapter 3. Data produced on the Alphastep cannot be exported as a chart thus all measurements were taken within the software. Data is displayed as a plot of stylus deflection as a function of lateral position on the sample while the stylus is dragged across step between the uncoated and coated regions of the sample. Two cursors can be placed on the surface profile and the height difference between those points is given. The

methodology for determining the coating was subject to surface roughness variations for the uncoated and coated regions. The data presented hereafter was produced by a software-managed average of ten 1000 μm scans across the step between the uncoated region and the various coated regions. Figure 4.1 is given without units as a sample surface profile for the purposes of clarifying the measurement methodology. The low region represents the uncoated surface, the upper region represents the coated surface, and the red lines indicate the reference points for film thickness measurements.

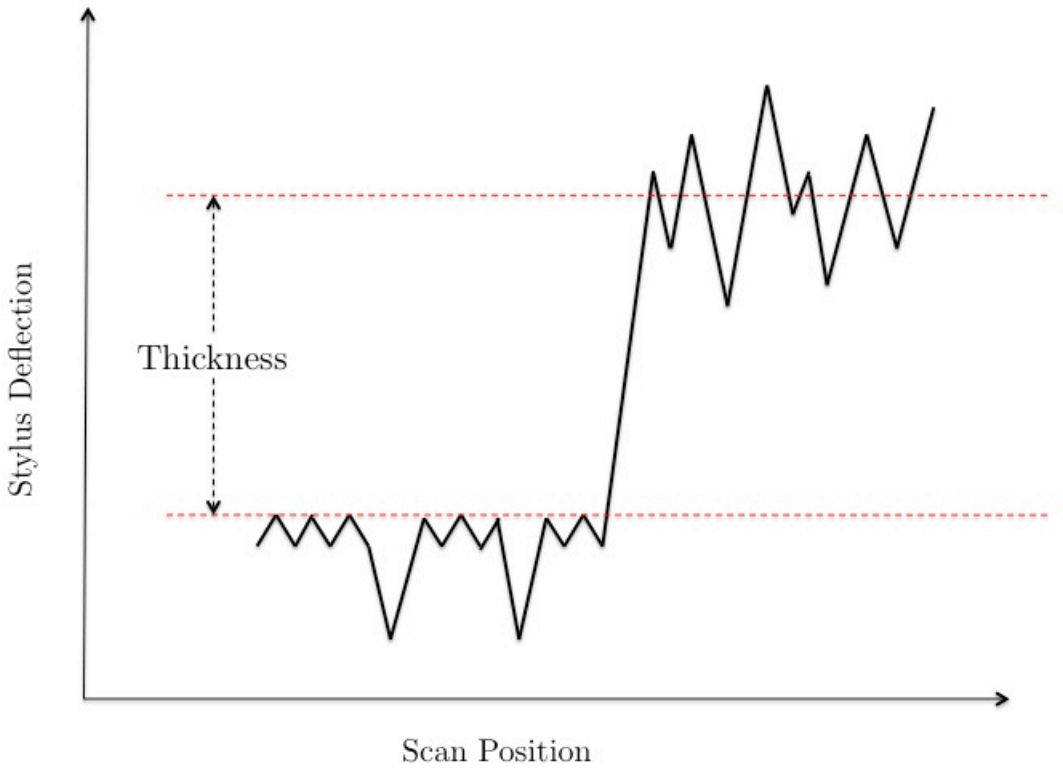

Figure 4.1 Example surface profile across the uncoated/coated step.

Surface variations on the uncoated region of the BC-404 sample were regularly spaced valleys with a depth of 150 +/- 20 nm. Due to their regular spacing, it is likely that these variations are an artifact of the milling process to manufacture the samples in the square geometry. Surface variations on the coated regions were 250 +/- 50 nm (peak to valley) and appeared to be independent of coating thickness. Regularity similar to that of the uncoated surface was not seen for the roughness on the coated regions.

Consistent measurements of the step height were difficult in light of the surface variations. The first cursor was maintained on the plateaus between valleys on the uncoated part of the profile. Step height measurements were extremely sensitive to the placement of the second cursor on the coated side of the profile. Variations of 250 nm, commensurate with the surface roughness of the coating, could be achieved based on the placement of the cursor. In order to take consistent, though potentially imprecise, measurements the second cursor was placed at the midpoint of the maximum peak-to-valley surface variation. This data is represented in Figure 4.2.

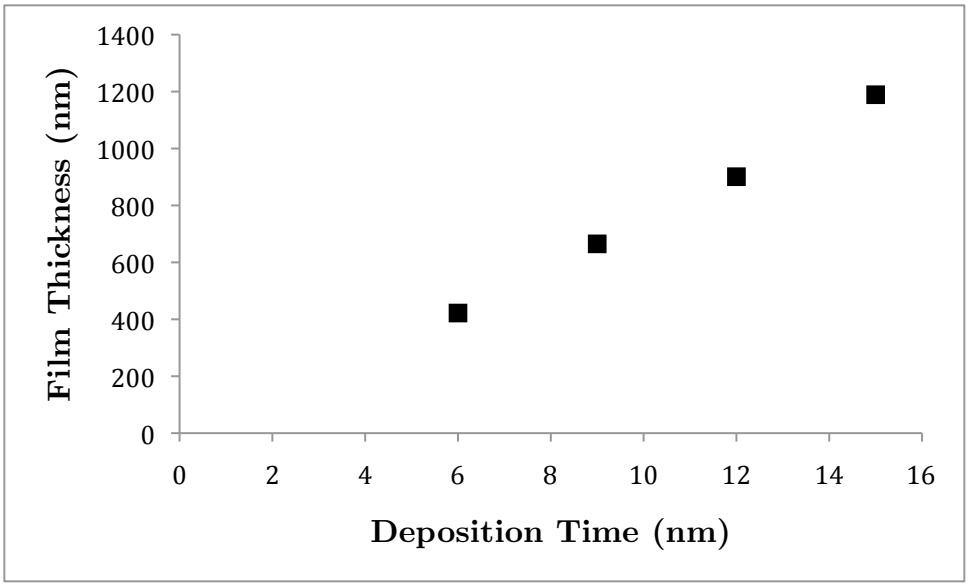

Figure 4.2 Film thickness as a function of deposition time for SiO_2 on a BC-404 substrate.

A linear least squares fit of this data, with a forced intercept at the origin, results in the equation

$$X(t) = 76.47t \tag{4.1}$$

where **X(t)** is the film thickness in nanometers and **t** is the deposition time in minutes. In contrast, this recipe was determined by other users to produce a deposition rate of 16 nm min^{-1} on a silicon wafer substrate. The R^2 for this fit is 0.98781. Data for the 3 minute deposition region is not given because magnitude of the surface variations was large compared to the expected coating thickness, thus the 3 minute coating was effectively irresolvable. Based on equation (4.1), the expected thickness for a 3 minute deposition is 230 nm.

Table 4.1 SiO_2 film thickness as a function of deposition time for PECVD deposition on BC-404 substrate.

Deposition Time (min)	Film Thickness (nm)
6	422
9	665
12	901
15	1189

It is also important to recognize that this deposition rate data is presented without an associated uncertainty. Measurement uncertainties on the Alphastep Tencor are unknown, however it must be conceded that the total uncertainty, based on the data acquisition constraints of the profilometer system, are likely substantial, especially at smaller thicknesses. Based on experimentation with the placement of the cursors, this uncertainty is estimated as 15-20% of the film thickness. Coated samples will hereafter be referred to by the film thicknesses presented in Table 4.1.

Data from the neutron activation analysis discussed in Chapter 3 are limited to the two samples tested. Both samples were coated for 6 minutes. Comparison of Tables 4.1 and 4.2 shows poor agreement between film thickness measurements from profilometry and neutron activation analysis.

Table 4.2 SiO_2 film thicknesses for identically coated BC-404 samples.

Sample NAA ID	Thickness (nm)
L0831	703
L0832	821

The systematic errors inherent to the NAA process were known before the experiment was conducted: even samples taped rigorously to isolate one face of the sample showed evidence of coating on other surfaces. This increased exposure would lead to a larger measured mass of silicon on the sample and inflate the calculated thickness. Additional considerations include variations in the exposed surface area due to non-identical sample geometries and high uncertainties associated with low count totals for both samples.

4.3 Relative Efficiency

Calculation of the absolute efficiency of each detector at each of the mixed gamma source energies allowed for the determination of the relative efficiency of the two detectors for a given sample geometry. Check sources were created, according to the procedure outlined in Chapter 3, to best replicate the geometries of the BC-404 and EJ-204 samples coated by SiO_2/Al_2O_3 and exposed to radioxenon. An example curve for the absolute efficiency of a detector is given in Figure 4.3.

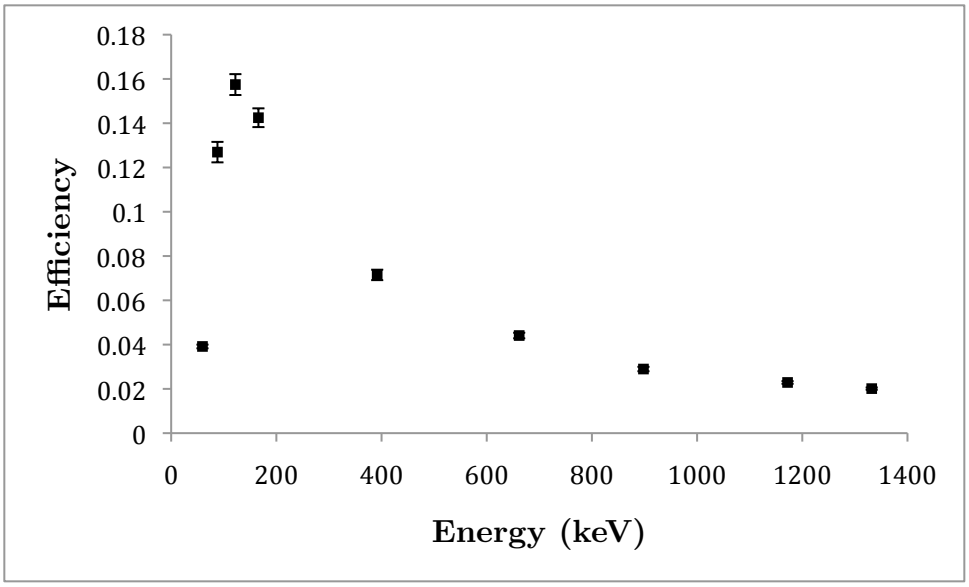

Figure 4.3 Absolute efficiency of the short right angle detector for the 1" square check source.

The data point size in Figure 4.3 has been reduced to make the error bars visible. Similar data sets were produced for the other detector used for sample counting, as well as for the 0.5" check source. It is important to note that the efficiency curve is steepest in the region 0-400 keV and associated uncertainty is largest in this region. We expect that fitting equations for this data will then be the least accurate in this region. The photopeaks of interest for this project are 81 keV, 188 keV, and 243 keV.

This data was mapped to a log-log graph then fit to a 4^{th} order polynomial. Manipulation of this polynomial led to an equation to describe the absolute efficiency as a function of energy with the form

$$Eff_{Abs.}(E) = \exp\left[C_1 \ln(E)^4 + C_2 \ln(E)^3 + C_3 \ln(E)^2 + C_4 \ln(E) + C_5 \right] \quad (4.2)$$

where $\mathbf{C_n}$ are the coefficients produced in the polynomial fit and **E** is the energy in keV.

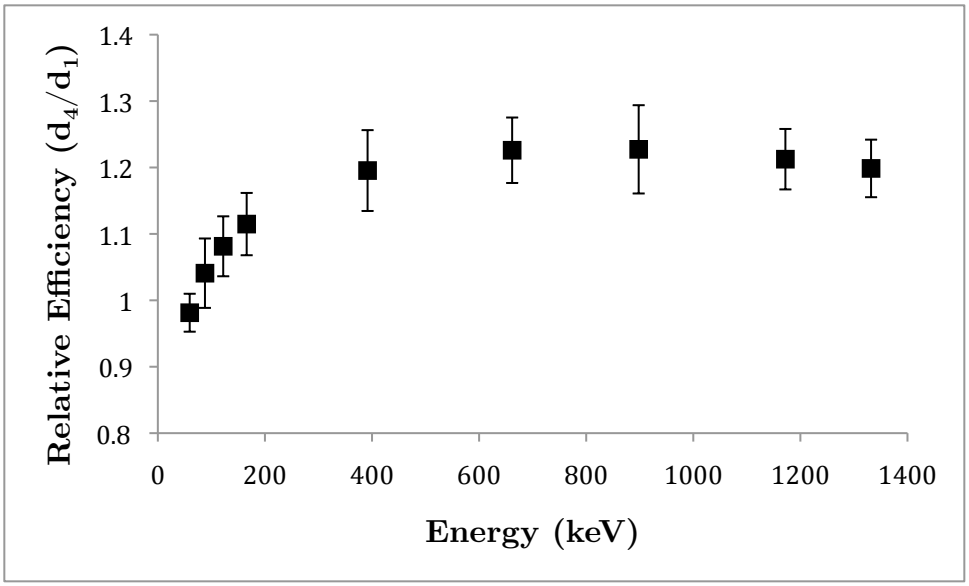

Figure 4.4 Relative efficiency data for detectors using the 1" square check source.

Figure 4.4 is given for the efficiency of the short right angle detector (d_4) relative to the green clamshell shield detector (d_1) using the 1" square check source. Both detectors are HPGe detectors in the NETL gamma spectroscopy lab. This data set was produced by comparison of the absolute efficiency, such as that given in Figure 4.3, of each detector at the energies used in the check source.

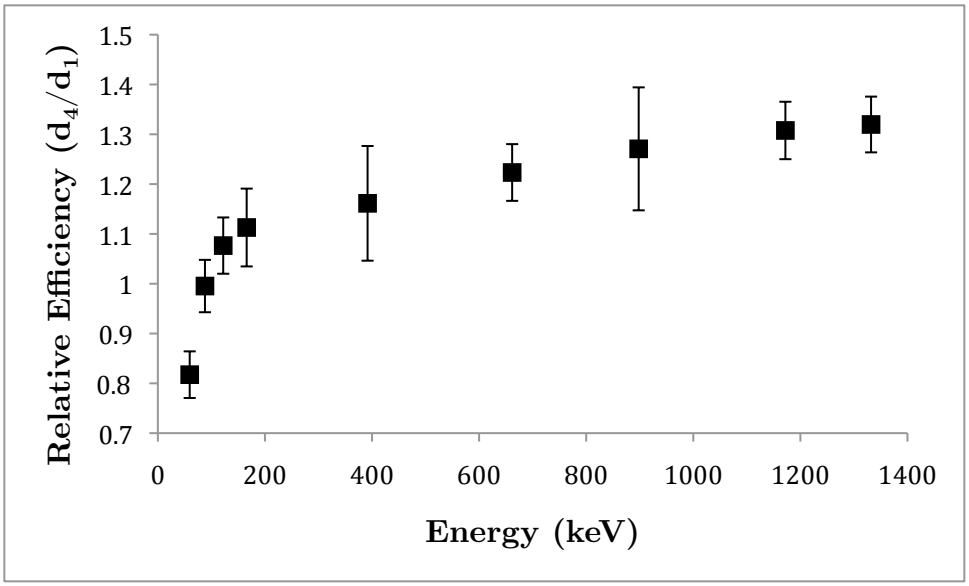

Figure 4.5 Relative efficiency data for detectors using 0.5" check source.

A similar set of data, given in Figure 4.5, was produced for the 0.5" check source. Of note is the fact that the relative efficiency for this check source differs substantially from that of the 1" check source, especially at very low and very high energies. This variation in relative efficiency as a function of check source geometry illuminates the importance of calculating the relative efficiency of a pair of detectors for geometry representative of the experimental sample geometry.

The uncertainty at each energy is shown by vertical error bars in the two previous figures. This uncertainty accounts for counting statistics in all the spectra used to calculate the relative efficiencies as well as uncertainty in the activity of the gamma emitters in the mixed gamma source used to produce the check sources. Variations in activity uncertainty were minimal relative to variations in the uncertainty from counting statistics. The larger uncertainties, such as those at 391 keV for ^{113}Sn and 898 keV for ^{88}Y, were a result of low count rates in the check source. Uncertainties for the 0.5" check source are larger,

relative to the 1" check source, as a result of lower count rates. This is attributable to the smaller volume of the mixed gamma solution deposited in the 0.5" check source, as detailed in Chapter 3 of this thesis.

4.4 Relative Activity

In order to verify the experiment, an exposure was run with two uncoated samples. For identical samples, the ratio of the count rates in each sample would provide an indication of inaccuracies in the relative efficiency curve or problems in the exposure process of the experiment.

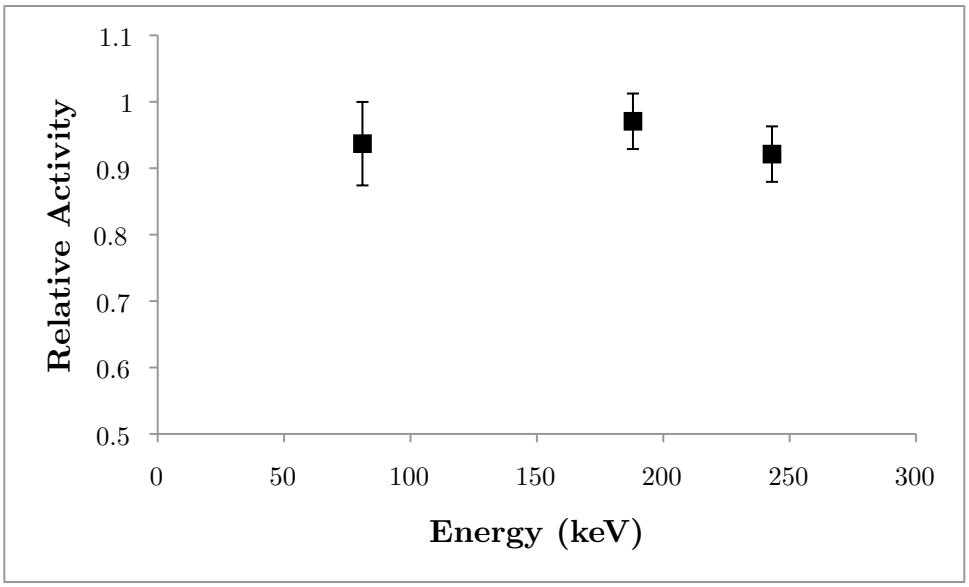

Figure 4.6 Relative activity of two uncoated square BC-404 samples.

For the 81 keV ^{133}Xe photopeak and the 188 keV ^{125}Xe photopeak, the relative activity ratio of the identically exposed uncoated samples is within σ of a ratio of 1, where σ describes the uncertainty associated with the relative activity

at each energy. The 243 keV ^{125}Xe photopeak is within 2σ of a ratio of 1. These results show good agreement with the expected ratio of count rates between the two detectors used for simultaneous measurement.

If the values of the relative activity for identical uncoated samples, given in Figure 4.6, are to be considered trending below the expected value of 1, it can be inferred that corrected efficiency of one detector is reliably lower than the efficiency of the other. The arrangement of samples was kept consistent throughout the experiments such that coated samples were always counted on the same detector. Based on this trend and the arrangement of samples, the additional correction would increase all the relative activities presented in this section.

Two exposures were conducted using coated EJ-204 square samples. One was coated for 3 minutes to produce a 230 nm SiO_2 film; the other was coated for 12 min to produce a 901 nm SiO_2 film.

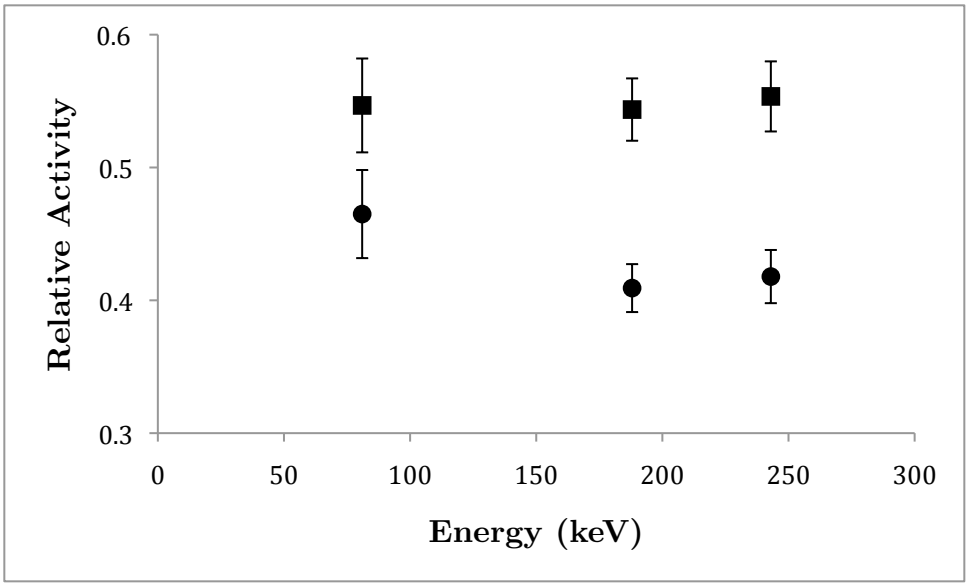

Figure 4.7 Relative activities for a 230 nm coated SiO_2 sample (square) and 901 nm coated SiO_2 sample (circle).

The 230 nm sample was exposed to radioxenon 2 days after coating while the 901 nm sample was exposed 7 days after coating. Both thicknesses show good agreement between the isotopes. The reduction in the memory effect is roughly 10% greater in the 901 nm sample than in the 230 nm sample. This suggests that the critical thickness for a SiO_2 diffusion barrier of xenon is larger than 230 nm. Relative activities and associated uncertainties are given in Table 4.4.

Two exposures were conducted using BC-404 endcap samples. One was coated with 20 nm Al_2O_3; the other was coated with 50nm Al_2O_3.

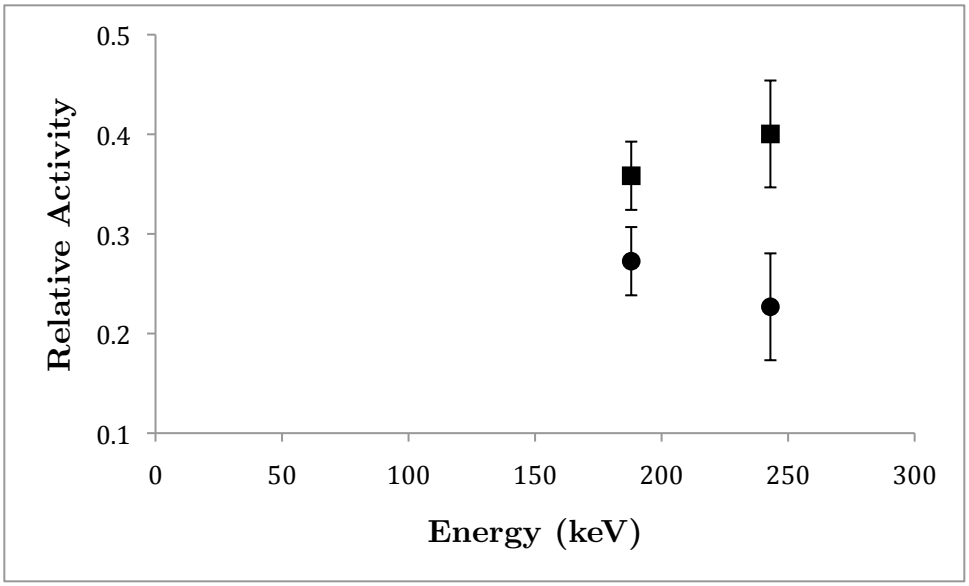

Figure 4.8 Relative activities for a 20 nm Al_2O_3 coated sample (square) and a 50 nm Al_2O_3 coated sample (circle).

The 20 nm sample was exposed to radioxenon approximately 150 days after coating. The 50nm sample was exposed to radioxenon approximately 30 days after coating. The 50nm sample reduced the memory effect by an additional 10-15% relative to the 20nm sample, suggesting that the critical thickness for an Al_2O_3 diffusion barrier for xenon is larger than 20 nm. Both samples showed good agreement between photopeaks. The count rate for the 81 keV ^{133}Xe photopeak was below the critical limit for one of the detectors used in the experiment, thus relative activity data is not available for that energy. Relative activity values and the associated uncertainties for the Al_2O_3 coated samples are given in Table 4.3.

One SiO_2 coated endcap was tested as well. The BC-404 cap was coated for 6 minutes to produce a 422 nm film.

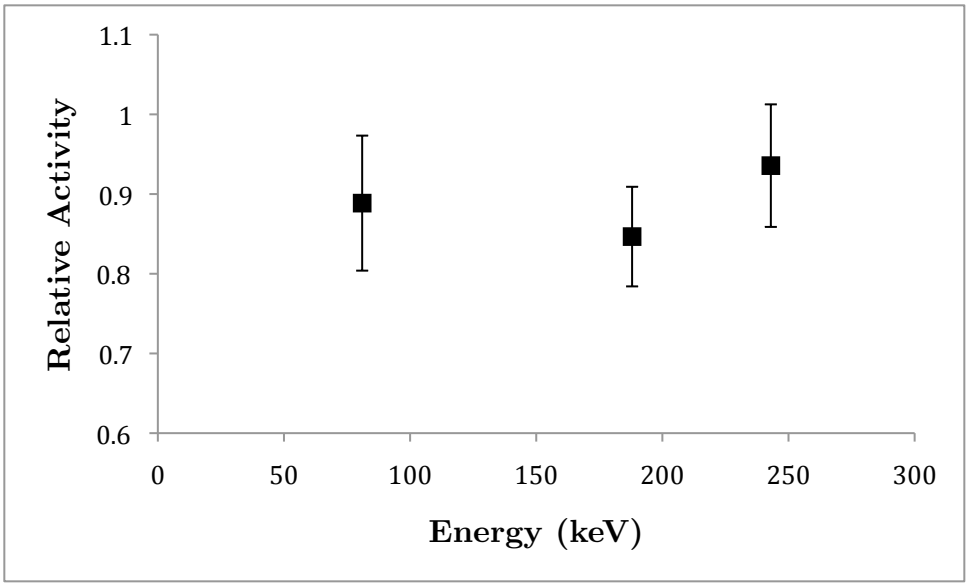

Figure 4.9 Relative activity of a 422 nm SiO_2 coated sample.

The 422 nm SiO_2 coated endcap was exposed to radioxenon approximately 130 days after coating. Relative to the other coated samples, the reduction in memory effect for this sample was much less pronounced. Relative activities are in agreement across the photopeaks, however values from 85% to 93% indicate that this SiO_2 film was not as effective in preventing diffusion as the other samples. Larger reductions were seen for thinner and thicker films of the same material and for films on the same geometry sample. The other SiO_2 coated samples were exposed and counted relatively quickly after the thin film was manufactured in the PECVD reactor, whereas this sample was left for over 4 months before exposure and measurement. This could indicate degradation of the film over time. It is important to note that comparable signs of degradation did not appear on Al_2O_3 coated samples that were counted within a similar timeframe as this SiO_2 sample.

Table 4.3 Relative activities and associated uncertainty (given in %) for 20 nm and 50 nm Al_2O_3 coated BC-404 endcaps.

	81keV ^{133}Xe	**188keV ^{125}Xe**	**243keV ^{125}Xe**
20 nm	n/a	35.8 +/- 3.4	40.0 +/- 5.3
50 nm	n/a	27.2 +/- 3.1	22.7 +/- 3.7

The data in Tables 4.3 and 4.4 indicate that thicker coatings are more effective at mitigating the memory effect. This result is expected for coating thicknesses below the critical thickness where thicker coatings are not increasingly effective. The 422 nm SiO_2 does not support this conclusion, however it is likely that the minimal reduction in memory effect seen for this sample is attributable to film degradation or another unforeseen effect.

Table 4.4 Relative activities and associated uncertainty (given in %) for 230 nm, 422 nm, and 901 nm SiO_2 coated samples.

	81keV ^{133}Xe	**188keV ^{125}Xe**	**243keV ^{125}Xe**
230 nm	54.7 +/- 3.5	54.4 +/- 2.3	55.4 +/- 2.6
422 nm	88.9 +/- 8.5	84.7 +/- 6.2	93.6 +/- 7.7
901 nm	46.5 +/- 3.3	40.9 +/- 1.8	41.8 +/- 2.0

It is also important to note that in all cases, the relative activities of each sample are in agreement across the ^{133}Xe and ^{125}Xe photopeaks. The result suggests that isotopic fractionation is not a significant mechanic in the diffusion of radioxenon through polymer.

Although agreement between isotopes was consistent and the relative activity for two uncoated samples was close to 1, quantitative uncertainty for the results was appreciable. In some cases the uncertainty exceeded 10% of the calculated relative efficiency. Sources of uncertainty included in calculation of the final values included:

- Published uncertainty in count rates for various isotopes in the mixed gamma source used for absolute efficiency calculations.
- Statistical uncertainty in the count rates for the background spectrum of each detector.
- Statistical uncertainty in the count rates for the 1" and 0.5" check sources used for relative efficiency calculations.
- Statistical uncertainty in the count rates for exposed samples.

Of these sources, the largest contribution towards the final uncertainty was the convolution of uncertainties calculated for the relative efficiency between detectors.

Additional systematic errors may have contributed to variation in the results, however these errors were not included in calculations of the uncertainties provided in Tables 4.3 and 4.4. Such errors could include variation in the position of the sample on each detector between experiments, differing concentrations of xenon between the test chambers as a result of differential

leakage out of one chamber, or reductions in the effective exposed surface area of samples as a result of optical cement spreading onto the surface. These sources of error were considered prior to the collection of data and, as a result, it is unlikely that the cumulative error from these systematic sources is substantial relative to the total statistical uncertainty presented with the final results.

Chapter 5: Conclusions

5.1 Summary

In Chapter 1, background material was presented to describe the development and significance of radioxenon monitoring as a method of verification for the Comprehensive Nuclear Test-Ban-Treaty. As part of the review of the literature, the radioxenon memory effect was identified as a problem in monitoring operations. Further review of diffusion barrier effectiveness and plasma enhanced chemical vapor deposition of thin films led to the conclusion that manufacture of thin film diffusion barriers by PECVD could serve as a means of mitigating the memory effect. The goals for the project were then outlined: to develop an apparatus capable of comparing the xenon activity in two plastic samples, to investigate deposition of thin films on plastic scintillator, and to quantify to ability of these thin films to mitigate the memory effect.

In Chapter 2, theory pertaining to the production of radioxenon was presented along with more detailed description of radioxenon monitoring equipment and techniques. A mathematical treatment of gas diffusion through a polymer, following the work done by Pressyanov [48], was provided in Section 2.3, followed by a description of PECVD reactor kinetics and SiO_2 film formation in Section 2.4.

Chapter 3 described the irradiation facilities at the University of Texas at Austin's NETL TRIGA reactor as well as procedures for producing radioxenon in the reactor. As part of the radioxenon production process, the use of the xenon transfer manifold was reviewed. The procedure for preparing a plastic

scintillator sample for exposure, as well as the use of the exposure manifold, was then outlined. Techniques for the measurement of relative efficiencies for a pair of detectors was given, including the process for creating check sources to replicate the sample geometry. The use of the PlasmaTherm 790 PECVD reactor at the University of Texas Microelectronics Research Center and the recipe for SiO_2 film production was described. Finally, steps were given to calculate the thickness of the PECVD deposited film using neutron activation analysis and contact profilometry.

Chapter 4 provided the results for the experiments detailed in Chapter 3. The performance of the exposure manifold was discussed along with results of the thin film characterization measurements using NAA and profilometry. Data was given for the absolute and relative efficiencies of the detectors for the two check source geometries. Finally, the relative activity of radioxenon for the coated samples was given to quantify the mitigation of the memory effect by each film. Sources of uncertainty in the final data were also described.

Chapter 5 gives a summary of the work done and describes how the goals of the project, given in Chapter 1, were met. Observations regarding the project and recommendations for future research conclude the work.

5.2 Project Goals

The initial goal for this project was to develop an experiment that would allow measurement of the radioxenon memory effect. The construction and high performance of the exposure manifold fulfilled the aspect of the goal regarding a suitable apparatus for the experiment. The procedures for radioxenon

production, sample preparation, and sample exposure, along with the results of the experiments given in Chapter 4, indicate that the development of an experiment was also successful, thus the first goal was comprehensively achieved.

The second goal was to investigate thin film deposition techniques and establish a procedure for thin film manufacture on plastic scintillator. PECVD was identified as a viable deposition technique based on initial testing. A procedure was developed to produce films on BC-404, however attempts at high precision characterization of the film were unsuccessful. Despite the inability to reliably quantify the SiO_2 films, relative activity results given in Chapter 4 clearly indicate that films that reduced the memory effect were being deposited. In this sense the rule of the second goal was met, though the spirit of the goal may not have been fully met in light characterization difficulties.

The third goal was to quantify the ability of the thin film diffusion barriers to mitigate the memory effect. Although the performance of each film was not entirely predictable, the diagnostic experiment conducted with identical uncoated samples indicated that the experimental techniques and data analysis methodology were effective in producing data with reasonable precision. In consideration of this diagnostic and the subsequent results for a variety of film thicknesses and materials, the third goal was achieved.

5.3 Observations and Recommendations

The first and foremost observation regards the results presented in Section 4.4. The Al_2O_3 barriers and SiO_2 barriers tested for this project were shown to be effective at reducing the memory effect by 45-65%, however it is

unlikely this reduction is substantial enough to make additional background counting in the INGE detectors unnecessary. In order to maintain the sensitivity required for the IMS, reductions in excess of 90% are likely required. In light of this, the results of this project certainly stand as progress towards the goal of fully mitigating the memory effect, however further work needs to be done.

It would be useful to produce a more extensive data set for both SiO_2 barriers and Al_2O_3 barriers. Both materials will have some critical thickness beyond which more material will not further reduce the memory effect. A larger distribution of film thicknesses would provide insight on these critical thicknesses. It has been seen in other studies [31] that the mechanical stress and likelihood of cracking increases as film thickness is increased. Even if >90% reductions are possible for either barrier, the requisite thicknesses may be so large that the films are not viable as a reliable, long-term solution to the memory effect problem. The results given in Figure 4.9 may indicate that unsustainable film thickness has already been reached, although it is entirely possible that this mitigation failure was the result of some other, unknown mechanic. An additional consideration in developing thicker films is the effect of the dead layer. Any material between the xenon gas and the plastic scintillator will absorb beta energy before the beta particles reach the scintillator without producing scintillation that can be detected in the PM tubes. The optimal film thickness may have to balance of the critical thickness with the effects of the dead layer. In all of these cases, a more comprehensive data set would be illuminating. With the procedures for barrier production and xenon exposure already described and tested, expansion of this data set can be considered an extremely reasonable goal.

Other data of interest would be relevant to the diffusion theory presented at the end of Section 2.3. Measurements of the radioxenon activity in samples for large decay times would allow the empirical calculation of the diffusion length of radioxenon in polyvinyltoluene. The model of radioxenon activity in the sample could then be used to estimate saturation and desorption timeframes, an especially useful calculation considering the automated measurement process in the INGE stations.

A final observation regarding the physics of radioxenon interacting with a polymer regards the assumption that diffusion is the sole mechanic driving the memory effect. This assumption is made for the purposes of this project. It is possible that intermolecular surface forces, capillary action, or other physical processes are also contributing to the memory effect in which case a simple monolayer diffusion barrier may not be sufficient for thoroughly reducing the memory effect. Calculations of the diffusion length using experimental data, as described in Section 2.3 and the previous paragraph, would absorb any other effects rather than identify them. In the absence of a diffusion barrier that sufficiently mitigates the memory effect, it may be worthwhile to investigate other contributions to the memory effect.

After the procedure for the PECVD deposition of SiO_2, it was discovered that previous work had shown that carrier gases improved the purity of films by decreasing the production of other species in the plasma [30]. As indicated by the PECVD recipe in Appendix C, a carrier gas was not used in the production of the films in this project. Development of a PECVD recipe for higher quality films may improve the effectiveness of the diffusion barriers.

Degradation of films over time was observed in the reference by Dameron et al [51]. An Al_2O_3-SiO_2 bilayer was produced in this reference and reductions in gas permeability by a factor of 10-150x were seen. Considering the ability of the MRC and collaborating Swedish facilities to produce monolayers of both of these materials, it may be of interest to investigate the effectiveness of such a bilayer in a xenon diffusion barrier application.

Considering the effects of film degradation observed in other references, as well as the implications such degradation would have regarding the usefulness of these films as a long term solution to the memory effect, it would certainly be necessary to investigate the ability of these films to reduce the memory effect over long periods of time. Intermittent exposure of the same coated sample, with sufficient time between exposures for the radioxenon to diffuse out and decay away, would be a simple way to produce this data. Characterization techniques may also be useful in exploring film degradation. More accurate profilometry, or the similar technique of atomic force microscopy, could detect substantial cracking. Other microscopy techniques, such as SEM, have been used [31] to qualify the mechanical integrity and overall quality of SiO_2 films. Similar characterization could be used to better tailor the manufacture process to the needs of this project.

Of all aspects of the project, the measurement of film thickness is likely the one that requires the most significant improvements. Neutron activation analysis stands as a unique method for verifying film thickness, however better control over the exposed surface area in the PECVD reactor is almost certainly necessary. Profilometry is likely the simplest technique for measuring thickness,

however the equipment available at the MRC is inadequate for high precision measurements. Higher quality profilometry equipment surely exists and the use of other facilities for this work may be necessary to improve the quality of the data.

A third characterization technique, ellipsometry, is not mentioned elsewhere in this thesis, however it was briefly explored as a means of measuring film thickness. An ellipsometer measures the change in polarization of light incident on a thin film and can calculate a number of optical properties of the film as a result. SiO_2 and polyvinyltoluene have indices of refraction that sufficiently similar that the ellipsometer was unable to resolve the film. It is not clear whether modifications to the sample or film, or use of an opaque proxy substrate, would enable the use of ellipsometry.

Considering the cylindrical geometry of the beta scintillator cells used in the INGE stations, even if a film is produced that shows sufficiently large reduction in the memory effect, the coating techniques that are currently used for small, flat samples would have be viable for the cylindrical geometries as well. Primarily, coating uniformity on the inner surface of the cylinder would have to be verified, presenting a new challenge for thickness verification. Field testing would also be required to ensure the integrity of the film over long periods of time so as to maintain the autonomous nature of the INGE stations.

It seems likely, in light of these initial experiments and data, that a diffusion barrier can be developed to sufficiently mitigate the memory effect such that background counting to account for the memory effect will no longer be necessary. Further work is required to prove this claim, however, and other

challenges would then need to be overcome before coated cells could be deployed in operating stations.

Appendix A

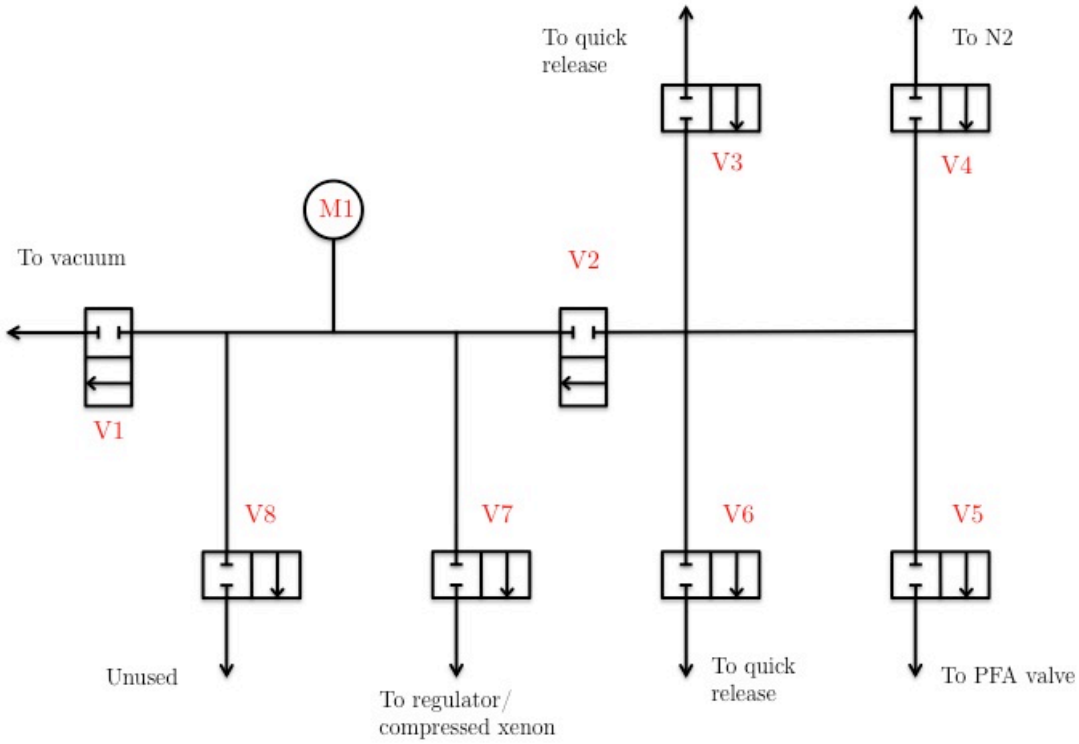

	V1	V2	V4	V5	V7	PFA	NV	Reg	XC
Attach PFA valve to V5	0	0	0	0	0	0	0	0	0
Evacuate manifold	1	1	0	1	1	1	0	0	0
N2 flush	0	1	1	1	1	1	0	0	0
Evacuate manifold	1	1	0	1	1	1	0	0	0
Isolate vacuum and N2	0	1	0	1	1	1	0	0	0
Release Xe to regulator inlet	0	1	0	1	1	1	0	0	1
Slowly feed xenon to regulator outlet	0	1	0	1	1	1	0	1	1
Set manifold at 1.3 bar Xe	0	1	0	1	1	1	1	1	1
Close Xe and isolate PFA valve	0	1	0	0	1	0	1	1	0
Isolate regulator	0	1	0	0	1	0	0	0	0
Return manifold to vacuum	1	1	0	0	1	0	0	0	0

Appendix B

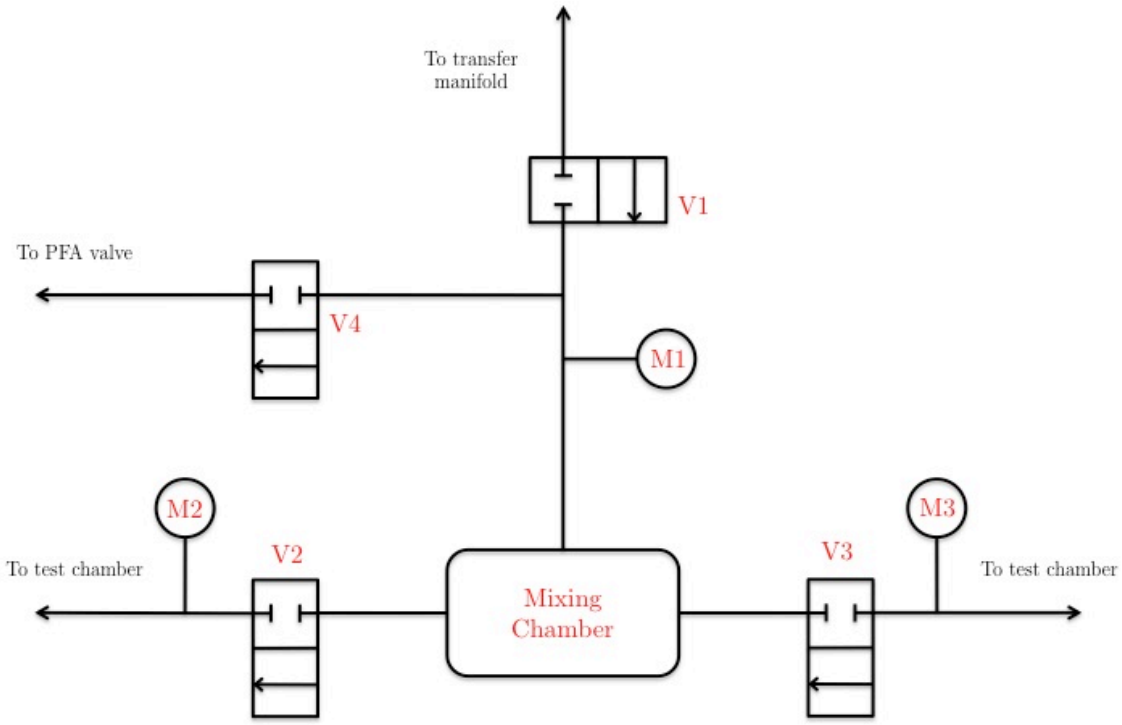

	V1	V2	V3	V4	PFA	From V1
Evacuate manifold	1	1	1	0	0	Vacuum
N2 flush	1	1	1	0	0	N2
Evacuate manifold	1	1	1	0	0	Vacuum
N2 backfill to 0.9 bar	1	1	1	0	0	N2
Isolate from transfer manifold	0	1	1	0	0	n/a
Open to PFA valve to verify seal	0	1	1	1	0	n/a
Open PFA valve to release Xe	0	1	1	1	1	n/a
Exposure	0	1	1	1	1	n/a
Test chamber removal	0	0	0	0	0	n/a

Appendix C

1. Initialize PECVD reactor at 60C and 800mTorr (1 minute)
2. N_2 flush at 500 mTorr (1 minute)
3. Evacuation (2 minutes)
4. N_2O – 160 sccm

   SiH_4 – 35 sccm

   1 minute 800 mTorr
5. N_2O – 160 sccm

   SiH_4 – 35 sccm
6. Evacuation (2 minutes)
7. N_2 flush at 500 mTorr (1 minute)

References

[1] U.S. Department of State. 1968. Treaty on the Non-Proliferation of Nuclear Weapons. *Treaties and other international acts series.* No. 6859.

[2] CTBTO Preparatory Commission. *Treaty Text.* http://www.ctbto.org/the-treaty/treaty-text/

[3] CTBTO Preparatory Commission. *Status of Signature and Ratification.* http://www.ctbto.org/the-treaty/status-of-signature-and-ratification/

[4] Hafemeister, D. 2007. Progress in CTBT Monitoring Since its 1999 Senate Defeat. *Science and Global Security* 15, no. 3: 151-183.

[5] CTBTO Preparatory Commission. *CTBTO Interactive World Map: IMS Radionuclide with Noble Gas.* http://www.ctbto.org/map/#ims

[6] Auer, M., A. Axelsson, X. Blanchard, T.W. Bowyer, G. Brachet, I. Bulowski, Y. Dubasov, et al. 2004. Intercomparison experiments of systems for the measurement of xenon radionuclides in the atmosphere. *Applied radiation and isotopes: including data, instrumentation and methods for use in agriculture, industry and medicine* 60, no. 6 (June): 863-77.

[7] Perkins, R.W., and L.A. Casey. 1996. Radioxenons: Their Role in Monitoring a Comprehensive Test Ban Treaty. *DOE/RL-96-51.*

[8] Bowyer, T.W., K.H. Abel, C.W. Hubbard, A.D. McKinnon, M.E. Panisko, R.W. Perkins, P.L. Reeder, R.C. Thompson, and R.A. Warner. 1998. Automated separation and measurement of radioxenon for the Comprehensive Test Ban Treaty. *Journal of Radioanalytical and Nuclear Chemistry* 235, no. 1-2: 77-81.

[9] Hayes, J.C., K.H. Abel, T.W. Bowyer, T.R. Heimbigner, M.E. Panisko, P.L. Reeder, J.I. McIntyre, R.C. Thompson, L.C. Todd, and R.A. Warner. 1999. Operations of the Automated Radioxenon Sampler/Analyzer – ARSA. *Proceedings of the 21st Seismic Research Symposium*: 249-260.

[10] Stocki, T.J., M. Bean, R.K. Ungar, H. Toivonen, W. Zhang, J. Whyte, and D. Meyerhof. 2004. Low level noble gas measurements in the field and laboratory in support of the Comprehensive Nuclear-Test-Ban Treaty. *Applied Radiation and Isotopes* 61, no. 2-3: 231-5.

[11] Dubasov, Y., Y. Popov, V. Prelovskii, A. Donets, N. Kazarinov, V. Mishurinskii, V. Popov, Y. Rykov, and N. Skirda. 2005. The APIKC-01 automatic facility for measuring concentrations of radioactive xenon isotopes in the atmosphere. *Instruments and Experimental Techniques* 48, no. 3 (May): 373-379.

[12] Ringbom, A., T. Larson, A. Axelsson, K. Elmgren, and C. Johansson. 2003. SAUNA—a system for automatic sampling, processing, and analysis of radioactive xenon. *Nuclear Instruments and Methods in Physics Research Section A: Accelerators, Spectrometers, Detectors and Associated Equipment* 508, no. 3 (August): 542-553.

[13] Auer, M., T. Kumberg, H. Sartorius, B. Wernsperger, and C. Schlosser. 2010. Ten Years of Development of Equipment for Measurement of Atmospheric Radioactive Xenon for the Verification of the CTBT. *Pure and Applied Geophysics* 167, no. 4-5 (January): 471-486.

[14] Hennig, W., W.K. Warburton, A. Fallu-Labruyere, K. Sabourov, M.W. Cooper, J.I. McIntyre, A. Gleyzer, et al. 2009. Development of a phoswich detector system for radioxenon monitoring. *Journal of Radioanalytical and Nuclear Chemistry* 282, no. 3 (July): 681-685.

[15] Milbrath, B.D., M.W. Cooper, L.S. Lidey, T.W. Bowyer, J.C. Hayes, J.I. McIntyre, L. Karr, D. Shafer, and J. Tappen. Radioxenon Atmospheric Measurements in North Las Vegas, NV. In *29th Monitoring Research Review: Ground-Based Nuclear Explosion Monitoring Technologies*: 779-786.

[16] Biegalski, K M Foltz. 2001. Automatic analysis algorithm for radionuclide pulse-height data from beta-gamma coincidence systems. *Journal of Radioanalytical and Nuclear Chemistry* 248, no. 3: 663-672.

[17] Rynes, J., K.M. Biegalski, P. Donohoe, and S. Biegalski. 2000. Automatic and Interactive Analysis Software for Beta-Gamma Coincidence Systems Used in CTBT Monitoring. In *Proceedings of the 22nd Annual DoD/DOE Seismic Research Symposium: Planning of Verification of and Compliance with the Comprehensive Nuclear Test Ban Treaty (CTBT), September 13-15, 2000.*

[18] Farsoni, A.T., D.M. Hamby, K.D. Ropon, and S.E. Jones. 2007. Two-Channel Phoswich Detector. In *Proceedings of the 29th Monitoring Research Review: Ground Based Nuclear Explosion Monitoring Technologies.*

[19] Cooper, M., J. McIntyre, T. Bowyer, A. Carman, J. Hayes, T. Heimbigner, C. Hubbard, L. Lidey, K. Litke, and S. Morris. 2007. Redesigned β–γ radioxenon detector. *Nuclear Instruments and Methods in Physics Research Section A: Accelerators, Spectrometers, Detectors and Associated Equipment* 579, no. 1 (August): 426-430.

[20] Saey, P.R.J., G. Wotawa, L.E. De Geer, A. Axelsson, M. Bean, R. D'Amours, K. Elmgren, et al. 2006. Radioxenon background at high northern latitudes. *Journal of Geophysical Research* 111, no. D17.

[21] Kalinowski, M.B, A. Becker, P.R.J. Saey, M.P. Tuma, and G. Wotawa. 2008. The Complexity of CTBT Verification. Taking Noble Gas Monitoring as an Example. *Complexity* 14, no. 1: 89-99.

[22] McIntyre, J.I., K.H. Abel, T.W. Bowyer, J.C. Hayes, T.R. Heimbigner, M.E. Panisko, P.L. Reeder, and R.C. Thompson. 2001. Measurements of ambient radioxenon levels using the automated radioxenon sampler/ analyzer (ARSA). *Journal of Radioanalytical and Nuclear Chemistry* 248, no. 3: 629-635.

[23] Chastgner, P. 1991. Elimination of "Memory" from Sample Handling and Inlet System of a Mass Spectrometer. *U.S. Patent A7-697,042.*

[24] Poths, J. 1995. A high efficiency ion source for Kr and Xe isotopic measurements. *International Journal of Mass Spectrometry and Ion Processes* 146-147 (August): 47-54.

[25] Seifert, C.E., J.I. McIntyre, K.C. Antolick, A.J. Carman, M.W. Cooper, J.C. Hayes, R. Heimbigner, et al. 2005. Mitigation of Memory Effects in Beta Scintillation Cells for Radioactive Gas Detection. In *Proceedings of the 27th Seismic Research Review: Ground Based Nuclear Explosion Monitoring Technologies*, 804-814.

[26] Ven, E.V. 1981. Plasma deposition of silicon dioxide and silicon nitride films. *Solid State Technology* 24, no. N-1: 167-171.

[27] Adams, A. 1983. Plasma deposition of inorganic films. *Solid State Technology* 26, no. 4: 135-139.

[28] Batey, J., and E. Tierney. 1986. Low-temperature deposition of high-quality silicon dioxide by enhanced chemical vapor deposition. *Journal of Applied Physics* 60, no. 9 (November): 3136-3145.

[29] Deshmukh, S.C. 1996. Investigation of low temperature SiO2 plasma enhanced chemical vapor deposition. *Journal of Vacuum Science & Technology B* 14, no. 2 (March): 738.

[30] Hsieh, S.W., C.Y. Chang, and S.C. Hsu. 1993. Characteristics of low-temperature and low-energy plasma-enhanced chemical vapor deposited SiO2. *Journal of Applied Physics* 74, no. 4: 2638-2649.

[31] Rats, D., V. Hajek, and L. Martinu. 1999. Micro-scratch analysis and mechanical properties of plasma-deposited silicon-based coatings on polymer substrates. *Thin Solid Films* 340, no. 1-2 (February): 33-39.

[32] Erlat, A.G., R.J. Spontak, R.P. Clarke, T.C. Robinson, P.D. Haaland, Y. Tropsha, N.G. Harvey, and E.A. Vogler. 1999. SiOx Gas Barrier Coatings on Polymer Substrates: Morphology and Gas Transport Considerations. *The Journal of Physical Chemistry B* 103, no. 29 (July): 6047-6055.

[33] Erlat, A.G., B. Wang, R.J. Spontak, Y. Tropsha, K.D. Mar, D.B. Montgomery, and E.A. Vogler. 1999. Morphology and gas barrier properties of thin SiOx coatings on polycarbonate: Correlations with plasma-enhanced chemical vapor deposition conditions. *Journal of Materials Research* 15, no. 3 (March): 704-717.

[34] D'Agostino, R., P. Favia, and F. Fracassi. 1997. Plasma processing of polymers. In *Proceedings of the NATO Advanced Study Institute on Plasma Treatments and Deposition of Polymers, May 19-June 2, 1996, Italy.*

[35] Graham, T. Roy. Inst. J., 1829.

[36] Barton, R.S. 1960. The permeability of some plastic materials to H2, He, N2, O2, and A. *Atomic Energy Research Establishment (United Kingdom).*

[37] Takeuchi, H. 1990. A jump motion of small molecules in glassy polymers: A molecular dynamics simulation. *Journal of Chemical Physics* 93, no. 3 (August): 2062-2067.

[38] Takeuchi, H., and R. Roe. 1991. Molecular dynamics simulation of local chain motion in bulk amorphous polymers. I. Dynamics above the glass transition. *Journal of Chemical Physics* 94, no. 11 (June): 7446-7457.

[39] Takeuchi, H., and R. Roe. 1991. Molecular dynamics simulation of local chain motion in bulk amorphous polymers. II. Dynamics at glass transition. *Journal of Chemical Physics* 94, no. 11 (June): 7458.

[40] Takeuchi, H., and K. Okazaki. 1990. Molecular dynamics simulation of diffusion of simple gas molecules in a short chain polymer. *Journal of Chemical Physics* 92, no. 9: 5643.

[41] Müller-Plathe, F. 1992. Molecular dynamics simulation of gas transport in amorphous polypropylene. *Journal of Chemical Physics* 96, no. 4: 3200-3206.

[42] Sok, R.M., H.J.C. Berendsen, and W.F. Van Gunsteren. 2010. Molecular dynamics simulation of the transport of small molecules across a polymer membrane. *Journal of Chemical Physics* 96, no. 6 (March): 4699-4704.

[43] Krishna P.K.V., and R.H. Boyd. 1992. Simulation of Diffusion of Small-Molecule Penetrants in Polymers correction based on uniform density is employed. *Macromolecules* 25, no. 1 (January): 494-495.

[44] Gusev, A.A., F. Müller-Plathe, W.F. van Gunsteren, and U.W. Suter. 1994. Dynamics of Small Molecules in Bulk Polymers. *Advances in Polymer Sciences* 116: 207-247.

[45] Klopffer, M.H., and B. Flaconneche. 2001. Transport Properties of Gases in Polymers: Bibliographic Review. *Oil & Gas Science and Technology* 56, no. 3 (May): 223-244.

[46] Flaconneche, B., J. Martin, and M.H. Klopffer. 2001. Transport Properties of Gases in Polymers: Experimental Methods. *Oil & Gas Science and Technology* 56, no. 3 (May): 245-259.

[47] Mair, R.W., M.S. Rosen, R. Wang, D.G. Cory, and R.L. Walsworth. 2002. Diffusion NMR methods applied to xenon gas for materials study. *Magnetic Resonance in Chemistry* 40, no. 13 (December): S29-39.

[48] Pressyanov, D., K. Mitev, S. Georgiev, and I. Dimitrova. 2009. Sorption and desorption of radioactive noble gases in polycarbonates. *Nuclear Instruments and Methods in Physics Research Section A: Accelerators, Spectrometers, Detectors and Associated Equipment* 598, no. 2 (January): 620-627.

[49] Hahn, G.J. 1983. Plastic Container with Decreased Gas Permeability. *U.S. Patent 4,552,791*, filed 12 November 1985.

[50] Misiano, C., E. Simonetti, and F. Staffetti. 1995. Thin Film Multilayer Structure as Permeation Barrier on Plastic Film. *U.S. Patent 5,462,779*, filed 2 March 1993.

[51] Dameron, A.A., S.D. Davidson, B.B. Burton, P.F. Carcia, R.S. McLean, and S.M. George. 2008. Gas Diffusion Barriers on Polymers Using Multilayers Fabricated by Al2O3 and Rapid SiO2 Atomic Layer Deposition. *Journal of Physical Chemistry C* 112, no. 12 (March): 4573-4580.

[52] Groner, M. D., F.H. Fabreguette, J.W. Elam, and S.M George. 2004. Low Temperature Al2O3 Atomic Layer Deposition. *Chemistry of Materials* 16, no. 4 (May): 639-645.

[53] Hirvikorpi, T., M. Vähä-nissi, T. Mustonen, and A. Harlin. Thin Inorganic Barrier Coatings for Packaging Materials. In *2010 PLACE Conference, April 18-21, 2010, Albuquerque, New Mexico.*

[54] Groner, M.D., S.M. George, R.S. McLean, and P.F. Carcia. 2006. Gas diffusion barriers on polymers using Al2O3 atomic layer deposition. *Applied Physics Letters* 88, no. 5: 051907.

[55] Lamarsh, J.R., and A.J. Baratta. 2001. *Introduction to Nuclear Engineering.* 3rd ed. New Jersey: Prentice Hall.

[56] Haas, D. 2008. *Production of β-γ coincidence spectra of individual radioxenon isotopes for improved analysis of nuclear explosion monitoring data.* PhD diss., University of Texas at Austin.

[57] Korea Atomic Energy Institute. 2000. *Table of Nuclides.* http://atom.kaeri.re.kr/

[58] Biegalski, S.R.F., M. Deinert, T.G. Saller, and B.B. Wooten. 2009. Modeling Radioxenon Production and Release Pathways. In *2009 Monitoring Research Review: Ground-Based Nuclear Explosion Monitoring Technologies*, 615-623.

[59] England, T.R., and B.F. Rider. 1993. Fission Product Yields: Fast Pooled Neutron Induced Fission, ^{235}U. *Los Alamos National Laboratory, LA-UR-94-3106, ENDF-349.*

[60] Knoll, G. 2000. *Radiation Detection and Measurement.* 3rd ed. John Wiley & Sons, Inc.

[61] Saint Gobain Crystals. 2005. *BC-400, BC-404, BC-408, BC-412, BC-416 Premium Plastic Scintillators Technical Data.* Saint Gobain Ceramics & Plastics, Inc.

[62] University of Texas Nuclear and Radiation Engineering Program. 2010. *NETL Access & Procedures.* http://www.me.utexas.edu/~nuclear/

[63] Aghara, S., and W. Charlton. 2006. Characterization and quantification of an in-core neutron irradiation facility at a TRIGA II research reactor. *Nuclear Instruments and Methods in Physics Research Section B: Beam Interactions with Materials and Atoms* 248, no. 1 (July): 181-190.

[64] Shapiro, C.S. *Scope 50 – Radioecology after Chernobyl.* http://www.icsu-scope.org/downloadpubs/scope50/chapter01.html

Vita

Alexander Gary Fay was born in 1987 in Longmont, Colorado to parents Paula Corrette-Fay and Gary Franklin Fay. He was raised in Tucson, Arizona and received a BS in Physics from the University of Arizona in May 2009. He enrolled at the University of Texas at Austin in August 2009.

Permanent email address: alex.g.fay@gmail.com

This thesis was typed by the author.